Redox Biology 54 (2022) 102351

Contents lists available at ScienceDirect

Redox Biology

journal homepage: www.elsevier.com/locate/redox

Mecheliolide elicits ROS-mediated ERS driven immunogenic cell death in hepatocellular carcinoma

Zhongren Xu [a], Jianqiang Xu [b], Shibo Sun [b], Wei Lin [a], Yongming Li [a], Qiuyue Lu [a], Fuwei Li [a], Zhibin Yang [a], Yunlong Lu [a], Wukun Liu [a,*]

[a] Jiangsu Collaborative Innovation Center of Chinese Medicinal Resources Industrialization, School of Medicine and Holistic Integrative Medicine, Nanjing University of Chinese Medicine, Nanjing, China

[b] School of Life and Pharmaceutical Sciences (LPS) & Panjin Institute of Industrial Technology (PIIT), Dalian University of Technology, Panjin, China

A B S T R A C T

The nonnegligible reason for the poor prognosis of hepatocellular carcinoma (HCC) is resistance to conventional chemotherapy. Immunogenic cell death (ICD) is a rare immunostimulatory form of cell death that can reengage the tumor-specific immune system. ICD can improve the clinical outcomes of chemotherapeutics by promoting a long-term cancer immunity. The discovery of potential ICD inducers is emerging as a promising direction. In the present study, micheliolide (MCL), a natural guaianolide sesquiterpene lactone, was screened out by the virtual screening strategies, identified as an inhibitor of thioredoxin reductase (TrxR) and was evaluated to have high potential to induce ICD. Here, we showed that MCL induced ICD-associated DAMPs (damage-associated molecular patterns, such as CRT exposure, ATP secretion and HMGB1 release). MCL significantly triggered the regression of established tumors in an immunocompetent mouse vaccine model, and induced ICD (DCs maturation, the stimulation of $CD4^+$, and $CD8^+$ T-cells responses) in vivo. Mechanistically, we found that the magnitude of ICD-associated effects induced upon exposure of HCC cells to MCL was dependent on the generation of reactive oxygen species (ROS)-mediated endoplasmic reticulum stress (ERS). In addition, the suppression of ROS normalized MCL-induced ERS, in contrast, the downregulation of TrxR synergized with the ERS driven by MCL. We also systematically detected the H_2O_2 generation using Hyper7 sensors in HCC cells exposed to MCL. Notably, MCL inhibited the development of HCC organoids. Collectively, our results reveal a potential association between the TrxR inhibitors and ICD, presenting valuable insights into the MCL-activated ICD in HCC cells.

1. Introduction

Primary liver cancer, or hepatocellular carcinoma (HCC), is the third most common cause of cancer-related deaths worldwide [1]. The main treatment of HCC focuses on surgical therapy, and it cannot be ignored that HCC treatment has also been dominated by chemotherapy [2,3]. Despite recent improvements in chemotherapy for HCC, the average five-year survival rate of HCC patients remains poor due to the high rate of recurrence. The major driver of HCC recurrence is chemotherapy resistance [4,5]. Stimulating intrinsic immunity with tumor cytotoxicity and inducing continuous immunological memory have become promising and potential strategies in several cancers. Clinical treatment combined with immunotherapy and chemotherapy has been widely recognized as a comprehensive therapy for the development treatment of HCC [6,7].

Immunogenic cell death (ICD) is a unique cell death model contributing to the elimination of residual tumor cells upon apoptosis triggered by chemotherapeutics agents [8]. ICD was first proposed in 2005 upon rejuvenation of the tumor-specific immune system after pretreatment with the anticancer agent doxorubicin (DOX) [9]. The mechanism by which chemotherapeutic agents induce ICD relies on the emission or exposure of the potential unique signals named DAMPs. DAMPs always present from dying cancer cells, which mainly include the exposure of ER-resident chaperone protein calreticulin (CRT) and heat-shock protein 70/90 (HSP 70/90) on the cell membrane, extracellular release of high-mobility group Box 1 (HMGB1), and secretion of adenosine triphosphate (ATP). ICD inducers are generally classified into Type I and Type II. Type I inducers cause ICD by activating on non-ERS-associated biomarkers (ERS, collateral effects of type I inducers), whereas type II inducers can trigger ICD directly by ROS-mediated ERS and are generally more efficient [10]. The complex interplay of ROS and ERS is widely thought to instigate and regulate the DAMPs. In response to ICD inducers, activation of ERS has been identified to be indispensable in the ICD approach, which possesses the ability to elicit the danger signals associated with the trafficking of DAMPs, and subsequently stimulate anticancer immune responses.

TrxR is a homodimeric flavoenzyme presenting a unique crucial selenocysteine residue at its carboxy terminus [68]. As a key reductase

* Corresponding author. School of Medicine and Holistic Integrative Medicine, Nanjing University of Chinese Medicine, Nanjing, China.
E-mail addresses: liuwukun0000@njucm.edu.cn, liuwukun0000@hotmail.com (W. Liu).

https://doi.org/10.1016/j.redox.2022.102351
Received 2 March 2022; Received in revised form 13 May 2022; Accepted 23 May 2022
Available online 28 May 2022

of the entire thioredoxin system containing NADPH, TrxR and thioredoxin (Trx), TrxR transfers the reducing equivalents from NADPH to oxidized Trx (the substrate of TrxR), playing a significant role in maintaining intracellular redox homeostasis [11,12]. TrxR, also known as an essential antioxidant enzyme, donates the reducing equivalents through the reduced Trx to scavenge excess ROS [13]. In recent years, TrxR has been widely regarded as a promising anticancer target based on the clinical biomarker characteristics of HCC, and the TrxR is overexpressed in malignant cancers compared to noncancerous tissues [14] (TCGA and GEPIA databases). Most TrxR inhibitors interact with TrxR by a covalent bond or a potent interaction with the C-terminal Sec 498 of the selenium-containing enzyme [15,16]. Compounds possessing the ability to inhibit TrxR can induce the apoptosis of cancer cells by eliciting the ROS-mediated ERS. Increasing attention has been given to the crucial role of TrxR in the ROS generation and the ERS associated with the dramatic increase in ROS levels.

Cancer cells experiencing ICD are characterized by DAMPs, and ROS-mediated-ERS is essential in the danger signaling of DAMPs [17,18]. It is well known that Trx system is closely involved in the scavenging redundant ROS and stopping further ROS-driven ERS [15]. Blocking the Trx system contributes to the improvements in the tumor immune microenvironment and the signaling pathways related to the immune modulation [19,20]. The Trx system is also uncoupled by the macrophage P2X7 in the ATP signaling, which activates inflammasomes through endosome-generated ROS [21]. For chemotherapy-inducing ICD, one gold *N*-heterocyclic carbene complex recently has been demonstrated as an ICD inducer that is functionally induced by inhibiting TrxR2 in mitochondria and eliciting increased oxidative stress [18]. Thus, TrxR is a potential mark of DAMPs in ICD, and inhibiting the activity of TrxR may exert beneficial effects for the ICD-inducing approach.

In this study, we investigated whether the compound MCL could induce ICD through the inhibition of TrxR. For the first time, we showed the direct evidence of the reaction between MCL and TrxR. Interestingly, the results of our study demonstrated that MCL can elicit apoptosis by targeting TrxR, trigger ROS-mediated ERS, and subsequently induce ICD in HCC cells. Notably, the knockdown of TrxR could increase the ROS level and augment ERS, further contributing to the signaling pathways of DAMPs. MCL significantly decreased the proliferation of HCC tumor organoids. What's more, MCL exhibited great anti-tumor effects and stimulated the immune response in C57BL/6 mouse tumor-bearing model.

2. Materials and methods

2.1. Materials

Cell Counting Kit (CCK-8) was purchased from Yeasen Biotech Co., Ltd. (Shanghai, China). The dulbecco's modified eagle medium (DMEM) and trypsin were purchased from Thermo Fisher Scientific Inc. (Waltham, USA). Fetal bovine serum (FBS) was purchased from Genial Biological Inc. (Brighton, CO 80601, USA). The intracellular TrxR kit, the glutathione reductase (GR) kit, and 1640 culture medium were obtained from Solarbio Science & Technology Co., Ltd. (Beijing, China). The ROS probes 2′,7′-dichlorodihydrofluorescein diacetate (DCFH-DA) and Dihydroethidium (DHE), the Apoptosis body kit, the 4′,6-Diamidino-2-phenylindole (DAPI) stain solution, the Calcium ion fluorescent probe (Fluo-4), the ATP assay kit, and the BCA kit were bought from Beyotime Biotech (Nantong, China). The Annexin V-FITC apoptosis kit was bought from Meilune Biotech Co., Ltd. (Dalian, China). The proteinase inhibitor cocktail was bought from APExBIO Technology LLC (Houston, USA). The ECL solution was bought from Yeasen Biotech (Shanghai, China). The Collagenase IV and DNase were bought from Sigma (Munich, Germany).

The siRNA sequences were designed following the method of previous research, and synthesized by GenePharma (Shanghai, China).

Monoclonal *anti*-TrxR, *anti*-GAPDH, anti-Alpha-Tublin, *anti*-Calnexin, *anti*-Grp78, *anti*-ATF-4, *anti*-eIF2α/Phospho-eIF2α, anti-Chop, *anti*-AIF, *anti*-caspase 9/Cleaved-caspase 9, *anti*-Bcl2, *anti*-Bax, anti-Cytochrome C, *anti*-HSP 70/90, *anti*-Calreticulin, *anti*-HMGB1 and HRP-conjugated secondary antibodies were purchased from Proteintech Group (Wuhan, China) and Wanlei Biotech Co., Ltd. (Shenyang, China). The rmGM-CSF and IL-4 were purchased from Novoprotein (Shanghai, China). Anti-mouse-CD11c-PE/APC, anti-mouse-CD80-APC/FITC, anti-mouse-CD86-FITC/PE, anti-mouse-CD4-APC, anti-mouse-CD3-FITC, anti-mouse-CD8-PE and anti-mouse-CD45-PerCP-cy5.5 were bought from Thermo Fisher Scientific Inc. (Waltham, USA). All antibodies were diluted following the instruction manual. Five cell lines (HepG2, Hepa 1–6, LO_2, Huh7 and Huh7R (lenvatinib-resistant) were cultured in DMEM medium (10% FBS).

2.2. Virtual screening process

Three public databases (ZINC, TCMSP and some commercial data) were used in our study, and to generate the original database (127695 hits). Then, all hits were imported into the Ligpre module for suitable preparations. The Pharmacophore module was used to generate pharmacophore hypothesis and define the pharmacophoric features using the TrxR inhibitors present. The hits were imported in the pharmacophore filters, which could generate the compounds possessing the structural properties of inhibitors mentioned above. Based on the combined screening process, the covalent docking module was conducted to analyze the binding of TrxR-ligand complexes.

2.3. Synthesis of intracellular TrxR probe, MCL and MCL reduction product (Re-MCL)

All chemicals and spectrally pure grade solvents were commercially obtained and were used without further purification. All products from chemical reactions were monitored by TLC. Intracellular TrxR green probe was synthesized following the previous method [22,23] (Fig. S1C). The MCL and Re-MCL were synthesized by our group [24] (Fig. S1A). The corresponding spectra were attached in the supplemental materials (Figs. S12–S17).

2.4. Cell viability assay

To measure viability of cells, cancer cells were seeded at 96-well plates in DMEM complete culture media. The cells were allowed to attach overnight. Then the cells were incubated with different concentrations of agents for indicated time (24 h, 48 h, or 72 h) before performing CCK-8 assay.

3. TrxR activity determination assay

3.1. Isolated TrxR activity

The purified TrxR was kindly provided by Prof. Jianqiang Xu and Prof. Wei Lin. All TrxR protein used in this study was generated from *E. coli* [63,64]. The TrxR was reduced by NADPH in room temperature for 5 min in 96-well plates. The various concentrations of MCL and Re-MCL were subsequently added for 2 h at room temperature. Then a fresh TE buffer (50 mM Tris-HCl, pH 7.5, 1 mM EDTA, 50 mL) containing 5, 50-dithiobis (2-nitrobenzoate) (DTNB, 2 mM) was prepared and added in the corresponding wells. The activity of TrxR was immediately determined at 405 nm using the microplate reader during the initial 3 min. The linear increase in absorbance 405 nm was presented the activity of TrxR. The same volume of DMSO (1%, v/v) was added as the control group and the activity was expressed as the percentage of the control. Two mutants (USec498 TrxR and Truncated form of TrxR) were also prepared and performed as described above [63].

3.2. Investigation of the reaction between MCL and TrxR

TrxR and its mutant variants were pre-reduced by 100 μM NADPH for 10 min and then incubated with 50 μM MCL for 2 h. After the pre-incubation, the samples were hydrolyzed by 12 M HCL at 100 °C for 4 h, and were separately loaded to desalting columns for exchanging the buffer salt to an acetonitrile solution with 0.5% formic acid. Subsequently, samples were concentrated by vacuum evaporation and then subjected to UPLC-ESI-Q6500 (SECIX, USA) for adducts detection.

3.3. Intracellular TrxR and GR activity

When the cells (HepG2 and Hepa 1–6) grew to 70–80% in 6 cm culture plates, treated with different concentrations of MCL for 24 h. Then, the culture was carefully discarded and washed twice with sterilized PBS. Then, the TrxR/GR activity was measured according to the protocol of the intracellular Test kits. The activity was expressed as the percentage of the control. The intracellular TrxR activity was also detected by the immunofluorescence, the TrxR green probe (final concentration: 10 μM) was freshly prepared, and incubated for 1 h to detect the intracellular TrxR activity of each group. In brief, the cells were seeded in the 12-well plates. The cells were allowed to attach, then treated with MCL (10 μM, 20 μM, or 30 μM), The same amounts of DMSO (1%, v/v) were added as the control group.

3.4. Cellular thermal shift assay

The cellular thermal shift assay (CESTA) was used to determine the binding capacity of compounds on the thermal stability of P-gp based on the theory that some molecules could interact with their target proteins [25,26]. In brief, HepG2 and Hepa 1–6 cells were cultured and harvested as high-intensity suspension in PBS with the proteinase inhibitor cocktail. Then, the liquid nitrogen was gently added and covered the tube containing the suspension into a freeze-thawing cycle for three times, which responded to lyse the cells. After centrifuging (12,000×*g*, 4 °C), the supernatant was carefully retained, divided equally into PCR tubes and co-incubated with MCL (30 μM) and vehicle control (DMSO) at room temperature for 60 min. After incubation, the tubes were quickly heated to various temperatures (58 °C, 62 °C, 66 °C, 70 °C, 74 °C, and 78 °C) in a metal bath for 5 min. Finally, after centrifuging, the supernatant was subjected to the western blotting analysis.

3.5. Determination of intracellular ROS generation

The intracellular ROS was measured by the flow cytometry and immunofluorescence. Briefly, the cells (HepG2 and Hepa 1–6) were seeded in 24-well plates and overnight cultured. After the cells adhered to the wells, the various concentrations of MCL (10 μM, 20 μM, or 30 μM) were added for 3 h. The antioxidant NAC was added at 4 mM as the pretreatment for 1 h. The 10 μM DCFH-DA probe was added for 20 min at 37 °C in the dark. After the corresponding post-processing, the fluorescence was detected by a flow cytometer (BD Biosciences, USA) and a fluorescence microscope (Leica DMi8, Germany) respectively.

3.6. Cell transfections for gene (TrxR) silencing

To knockdown TrxR expression, HepG2 and Hepa 1–6 cells were plated in 6 cm plates at a density of 2×10^6 and cultured for 24 h. The siRNAs targeting TrxR and non-targeting control were transfected at a final concentration of 50 pM using siRNA-Mate reagent (GenePharma, Shanghai, China). After incubation for 6 h, the culture medium was replaced with fresh complete DMEM medium, and the cells were incubated for an additional 36 h. After 36 h post transfection, the TrxR expression in HepG2 and Hepa 1–6 cells was confirmed by Western blotting analysis. The siRNA oligonucleotides were synthesized by GenePharma. Si-TrxR1 (Sense: 5′-GCAAGACUCUCGAAAUUAU-dTdT-3'; antisense: 5′-AUAAUUUCGAGAGUCUUGC-dTdT-3′), Si-TrxR2 (Sense: 5′- GUGGGUUGCAUACCUAAGATT-dTdT-3'; antisense: 5′-UCUUAGGUAUGCAACCCACTT-dTdT-3′). After the sequence confirmation, the cells were treated with 30 μM MCL for different times and used for further assays.

3.7. Lentiviral transduction and transient transfection of Hyper sensor

The precise localization and accurate analysis of H_2O_2 generation in living cells are necessary. The stable HCC cell lines expressing Hypercytol, Hypernuc, Hypermito, Hyperpero, HyperER were constructed using lentiviral transduction [27,28]. For transfection experiments, 2×10^5 cells (HepG2 and Hepa 1–6) were grown overnight in six-well plates and transfected with different Hyper variants for another 48–72 h before adding the accessory reagents (A and B, auxiliaries in transfection) (BrainVT A (Wuhan, China) Co., Ltd). The best transfection efficiency was subsequently confirmed (MOI = 150).

For monitoring and analyzing the H_2O_2 signals in different Hyper variants in the presence or absence of MCL, all samples were acquired using the flow cytometer and immunofluorescence. After recording the Hyper signals, the data were analyzed using FlowJo and Fiji software, respectively.

3.8. Electron microscopy

HepG2 cells were cultured in 6-well plates with the corresponding treatment. NAC pretreatment (4 mM) where applicable was carried out for 1 h. Then the cells were harvested and fixed in phosphate buffer (pH 7.4) containing 2.5% glutaraldehyde overnight at 4 °C. The cells were post fixed in 1% OsO_4 at room temperature for 60 min, stained with 1% uranyl acetate, dehydrated through graded acetone solutions, and embedded in epon. Areas containing cells were block mount, cut into 70 nm sections, and examined with the electron microscope. An Olympus EM208S transmission electron microscope (TEM) was used to observe.

3.9. ATP release assay

The two cells (HepG2 and Hepa 1–6) were cultured in 6-well (2×10^5 cells per well) plates with the corresponding treatment. The intracellular and extracellular ATP levels were examined by ATP assay kits.

3.10. Measurements of cytosolic Ca^{2+}

To evaluate the steady state of cytosolic Ca^{2+} in cells (HepG2 and Hepa 1–6) after different concentrations of MCL treatments, the diluted Fluo-4/AM probe solution (final concentration: 2 μM) was added in each well of 12-well culture plates in the dark for 30 min at room temperature. After washing by PBS, the cytosolic Ca^{2+} level was immediately observed by a fluorescence microscope. The cytosolic Ca^{2+} level was expressed as the mean Fluo-4 fluorescence intensity. The accurate Ca^{2+} release was measured in the FLIPR Penta High Throughput Cellular Screening System, following the manufacturer's instruction of FLIPR Calcium 6 assay kits.

3.11. Immunofluorescence staining

The cells (HepG2 and Hepa 1–6) were overnight cultured in 12-well (5×10^4 cells per well) culture plates. After attaching, the cells were treated with 30 μM MCL and cultured for 24 h. NAC pretreatment (4 mM) where applicable was carried out for 1 h. All samples were firstly fixed and blocked. After incubating with the corresponding diluted antibodies overnight at 4 °C, the secondary antibodies conjugated with fluorophores were added. Then, the cells were washed with PBS for three times. The nuclei were counterstained by DAPI, if required. For the tissue slide, immunofluorescence staining was conducted on the frozen section of the tumor by fixation, permeabilization and blocked with 1%

BSA. Then the samples were incubated with the corresponding antibodies overnight at 4 °C, and the secondary antibodies conjugated with fluorophores were added. Nuclei were counterstained with DAPI. Immunofluorescence was detected with a fluorescence microscope (Leica, Dim8).

3.12. Flow cytometric analysis

After the cells (HepG2 and Hepa 1–6) attaching in 6-well (2×10^5 cells per well) culture plates, the various concentrations of MCL in the presence or absence of 4 mM NAC (pretreatment for 1 h) were added for 24 h. According to the demand of the experiments, the corresponding antibodies were diluted and added in wells. The secondary antibodies conjugated with fluorophores were added after recovering the primary antibody. Then, the staining cells were obtained and analyzed by a BD C6 plus flow cytometer, and the data was further analyzed with the FlowJo software.

3.13. Cell apoptosis analysis

HepG2 and Hepa 1–6 cells were treated with MCL (10 μM, 20 μM, or 30 μM) in the presence or absence of 4 mM NAC (pretreatment for 1 h) for 24 h in 6-well culture plates. The cells were then harvested and washed twice with PBS. The apoptosis cells were evaluated by double staining cells with FITC conjugated Annexin V and PI for 10 min in room temperature. Then, the staining cells were obtained and analyzed by a BD C6 plus flow cytometer, and the data was further analyzed with FlowJo software.

The degree of apoptosis was also assessed according to the number of apoptotic bodies observed by the immunofluorescence. In brief, the cells culture and agents treated were consistent with methods above. The Hoeschst dye was subsequently diluted and added into each well to incubate for corresponding time following the dye instructions. The apoptosis body was observed by the fluorescence microscope.

3.14. Western blot analysis

Total proteins from cells and tumor tissues were extracted by RIPA + PMSF (100: 1) buffer. The protein levels were quantified using the BCA protein assay kit. Equal amounts of protein in each group were separated by 10% SDS-PAGE and transferred to poly-vi-nylidene difluoride (PVDF) transfer membranes. The blots were blocked for 2 h at room temperature with freshly prepared 5% non-fat skimmed milk in TBST and then incubated with specific corresponding diluted antibodies at 4 °C overnight. After washing with TBST for three times, the membranes were incubated with the HRP-conjugated secondary antibody for 2 h at room temperature. ECL solution was used to visualize the bands and the signals were recorded by the chemiluminescence imaging analysis system (Azure Biosystems, California, USA).

3.15. In vitro DCs maturation assays

The DCs were freshly isolated from the bone marrow of C57BL/6 mice (3–5 weeks) following the previous study, with minor modifications [29,30]. In brief, the mice were firstly euthanized and disinfected with 75% alcohol for 15 min. The tibia and femur were stripped, then the bone marrow was immediately flushed out using fresh 1640 culture medium. After lysing the red blood cells, the purified bone marrow cells were seed in special 1640 medium containing rmGM-CSF (20 ng/mL) and IL-4 (20 ng/mL) in 24-well culture plates (1×10^6 cells per well). On day three, half of the culture medium in plates was replaced with an equal volume of fresh culture medium. The immature DCs were obtained after seven days culture.

The Hepa 1–6 cells were firstly seeded in the 24-well culture plate overnight. The various concentrations of agents were added for 24 h. Then the immature DCs were seeded into the *Trans*-well inserts (pore size of 1.0 μm) and cocultured with the treated Hepa 1–6 cells in *Trans*-well system for 24 h. The DCs were collected and analyzed by a BD C6 plus flow cytometer. Mature DCs were defined as $CD11c^+$ $CD80^+$ $CD86^+$.

3.16. In vivo tumor vaccination assay

All C57BL/6 mice (male, 3–5 weeks) were maintained in pathogen-free conditions and in vivo experiments were performed in accordance with the Guide for the Care and Use of Laboratory Animals (National Institutes of Health, the USA).

The Hepa 1–6 cells were treated with MCL (30 μM) and DOX (positive control, 0.8 μM) for 24 h, the same volume of DMSO served as the control group. Then the treated cells were harvested and resuspended in DMEM (FBS-free) culture medium. For vaccination, 200 μL of resuspended cells (2×10^6 cells per mouse) were injected subcutaneously to the right axillary as the primary tumor. After seven days, the vaccinated mice were re-challenged subcutaneously with 200 μL untreated Hepa 1–6 cells (2×10^6 cells per mouse) in left axillary as distant tumor. The volumes of the rechallenged tumors were monitored regularly by a digital caliper following formula TV (mm^3) = $width^2$ (length/2). Tumor volumes and body weights were recorded. The experiment would be stopped as soon as the mice become unmanageable (Mice bearing tumor burdens over 20–25% of the body weight).

3.17. Determination of in vivo tumor inhibitory efficacy of MCL treatment

In brief, the Hepa 1–6 cells were freshly prepared and harvested. 200 μL of Hepa 1–6 cells (2×10^6 cells per mouse) was injected subcutaneously to the right axillary as the primary tumor. When the primary tumors grew to approximately 100 mm^3, the mice were grouped randomly and treated with MCL (25 mg/kg) and DOX (1 mg/kg) (intraperitoneal injection). The tumor volume and mice weight were recorded. Finally, mice were sacrificed for blood, organs, and tumor collection. The tumors samples were divided into two parts, one for immunofluorescence staining and the other for flow cytometric analysis part. Collagenase IV (1 mg/mL) and DNase I (1 μg/mL) were used for digesting. Mature DCs were defined as $CD11c^+$ $CD80^+$ $CD86^+$. The percentage CTLS ($CD45^+$ $CD3^+$ $CD8^+$) and Th ($CD45^+$ $CD3^+$ $CD4^+$) cells were analyzed by flow cytometry. After the serum isolation, the interferon gamma (IFN-γ) and tumor necrosis factor alpha (TNF-α) in the sera of mice were also determined by the ELISA assays (Neobioscinece, Co., Ltd. China). Tumors from mice were immune-stained for H&E (histological examination) and TUNEL. The TrxR activity of tumor samples were analyzed, and the ROS generation were further investigated by two probes (DCFH-DA and DHE). The DAMPs and ERS related antibodies were used to investigate the tumor samples. The toxicity evaluation was subsequently performed, the main organs (heart, lung, liver, spleen, and kidney) were isolated and then harvested for H&E.

3.18. The assessment of anti-angiogenesis effects of MCL in zebrafish embryo development

The dechorionated zebrafish embryos 24 h post-fertilization were administered with different treatments for another 24 h culture. Embryos were tranquilized (0.03 mg/mL tricaine) for live imaging investigation of vessel defects with a fluorescence microscope. Then, the hatching rate and survival rate were calculated and statistically analyzed.

3.19. Determination of MCL treatment against HCC organoid model viability

HCC organoids model was freshly prepared and conducted [31,32]. Then, these organoids were added with different treatments. DMSO group performed as the negative control, and the two clinical drugs

(5-Fluorouracil and Oxaliplatin) were used as positive controls in 10 μM. MCL treatment was carried out in a concentration manner (1 μM, 10 μM and 50 μM). All groups were cultured for six days. The number and the size of organoids were analyzed under a microscope (Zeiss, Axiovert. A1) every three days.

4. Results and discussion

4.1. Screening potential TrxR inhibitors from integrative databases

A collection of small-molecule compounds was prepared for optimization. These compounds were imported to prepare in Ligand docking wizard with the Schrödinger Maestro software and translated into

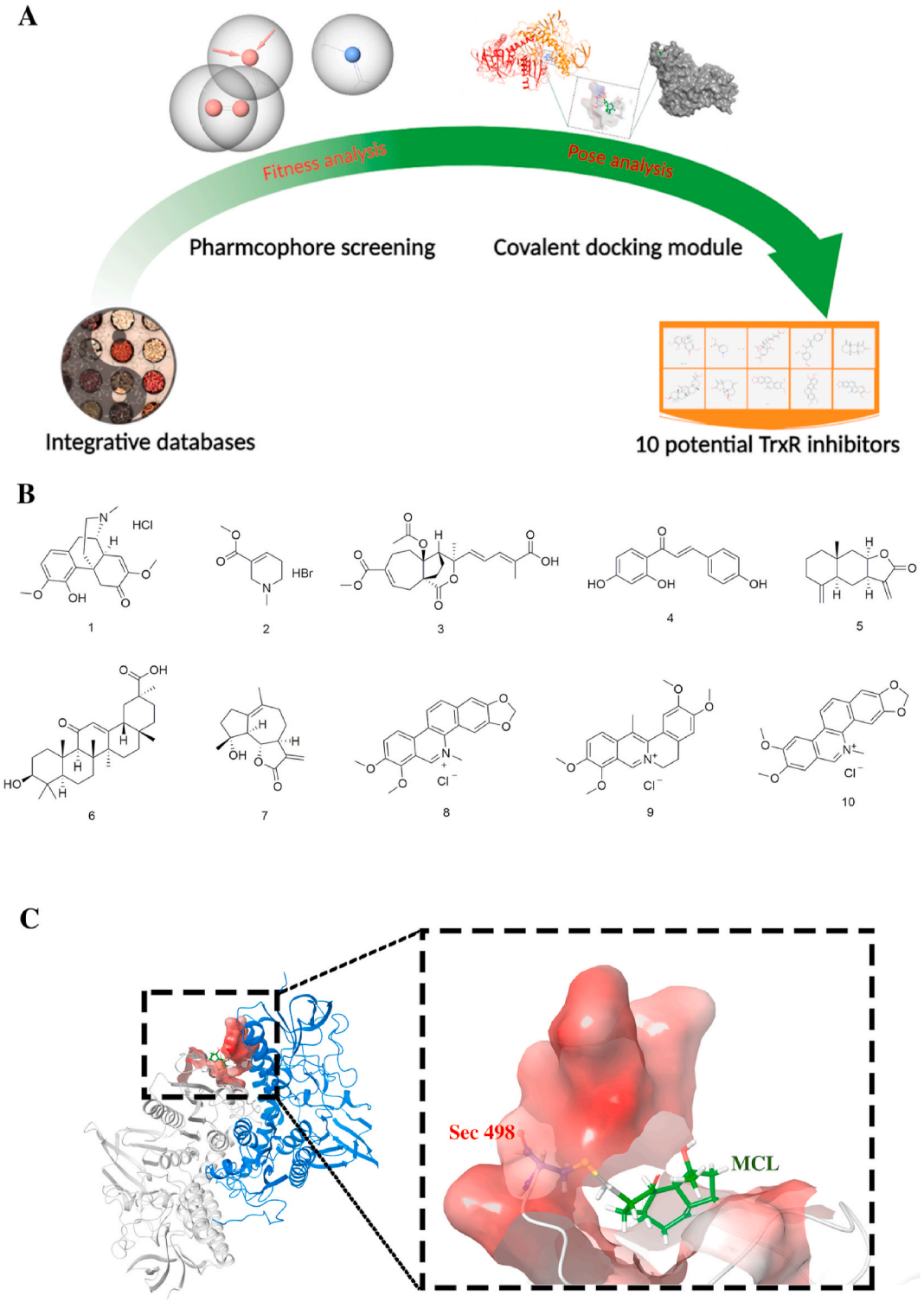

Fig. 1. The comprehensive screening process of TrxR inhibitors. (A) The screening process of discovering potential TrxR inhibitors from TCM database. The figure was created with BioRender.com. (B) Ten potential TrxR inhibitors were finally screened out and their structures were exhibited. (C) The key reaction between the Sec residue of TrxR and MCL were displayed by the molecular docking.

canonical SMILES for further analysis. According to the binding model of the TrxR inhibitor, it is universally recognized as a covalent bond between Sec 498 of TrxR and the α, β-unsaturated carbonyl groups of inhibitors [33,69]. Some new scaffold binding models were also found, such as an electrophilic center phenanthridinium group of sanguinarine [34] and chaetocin forming two hydrogen bonds with Glu477 of TrxR [35]. Then, the phase module of pharmacophore was used to generate and define the three pharmacophoric features mentioned above. The structural characterization of 127695 compounds was analyzed, and 3269 hits were selected and consistent with the "TrxR binding" rules. The covalent docking model was subsequently performed based on the templates of XP. The predicted binding affinity was temporarily identified to reflect the real binding model. According to the comprehensive evaluation, ten compounds were finally selected (Fig. 1A and B) and tentatively considered as the potential TrxR inhibitors. Among these hits, seven compounds contained the α,β-unsaturated carbonyl group, and others belonged to the alkaloids containing nitrogen.

To investigate the TrxR inhibition efficacy of ten potential hits, the validation experiments were performed, including wild type TrxR inhibition, TrxR mutant (USec498) inhibition and intracellular TrxR inhibition. To allow for rapid screening of hits, all compounds were prepared at a final concentration of 50 μM. As shown in Table 1, only Compounds 4, 5, and 7 presented some inhibition activity (approximately 80%). The carbon-terminal of TrxR is Sec 498, which possesses the significant reduced ability as the redox active-site and is generally considered as the key binding site of TrxR inhibitors. The mutant TrxR enzyme was established; the Sec residue was artificially removed and named TrxR (USec498). As we expected, the results of enzyme assays accounted for three promising hits that hardly reacted with the TrxR variant (USec498). Discovering selective TrxR inhibitors with desirable pharmacological properties in cancer cells is rational. We first investigated the *anti*-HepG2 effects of three hits. The intracellular TrxR assay was subsequently carried out, of which only Compound 7 (MCL) exhibited complete suppression of TrxR activity. Additionally, the binding pose analysis is shown in Fig. 1C. MCL could anchor the active pocket by a covalent bonding with the key Sec 498 of TrxR [33].

MCL, as a natural active compound with therapeutic efficacy toward inflammation and multiple cancers, belongs to guaianolide sesquiterpene lactone, which has been identified as the derivative of parthenolide (PTL) discovered in the flowers of Michelia compressa and Michelia champaca plants [36,37]. With better stability than PTL, MCL can selectively inhibit the activity of acute myelogenous leukemia stem and progenitor cells. As a compound of sesquiterpene lactone, the pharmacophore α-methylene-γ-lactone can react with biological nucleophiles.

4.2. MCL selectively inhibits TrxR activity and induces ROS generation

TrxR is a key selenoprotein containing a redox-active Sec 498 that is essential for enzymatic function, and has been proven to be significantly overexpressed in human HCC samples. Increasing interest has been attracted to discovering TrxR inhibitors for treating HCC [11,38]. Our results accounted for the fact that MCL contains an active (α-methylene-γ-lactone) moiety that may react with accessible Sec through a Michael-type addition reaction. Before the TrxR inhibition investigation, we tested the *anti*-HCC ability of MCL. As shown in Fig. 2A and B, MCL reduced the viability of HCC cells at different time points. The IC_{50} values were also calculated. Next, the TrxR assay was carried out to validate the inhibition efficiency of MCL. The concentration dependence (0–40 μM) of MCL is shown in Fig. 2C, MCL almost completely inhibited the TrxR activity at the concentration of 40 μM. The curve of kinetic studies was subsequently made with various concentrations (Fig. 2D), showing a linear relationship ($Y = -0.0026x + 0.0324$, $R^2 = 0.9909$), and the EC_{50} value of MCL toward TrxR was 6.23 μM. The loss of TrxR inhibitory activity of MCL might be due to reducing the double bond of the active moiety or Sec depletion mutant of TrxR (USec498) (Fig. 2E). The double bond of active moiety in MCL was also reduced, and the generated molecule (named Re-MCL, Fig. S1B) did not show TrxR inhibition (Fig. 2F) and had no antitumor activity against HCC cells (Fig. S1D). The inhibition of MCL against TrxR was totally lost due to the mutations of site Sec 498 in TrxR. To confirm the binding affinity between TrxR and MCL, the CESTA assay was further conducted. As shown in Fig. 2G and H, the expression level of TrxR remaining in the cellular soluble fraction decreased quickly when HepG2 and Hepa 1–6 lysates were heated from 58 to 78 °C. When the lysates were incubated with MCL (30 μM), the melting temperature of TrxR displayed a differential increase. However, the MCL had no effect on the thermal shift of the GAPDH level in either cell line in the CESTA assay (Figs. S1E and S1F).

To investigate the reaction between MCL and TrxR, we performed a validation assay by the mass detection. After incubating MCL with three TrxR mutant variants, all the complexes were hydrolyzed, respectively. All the hydrolyzed samples were analyzed by the UPLC-DAD-MS system. The theoretical molecular weights of MCL, Cys, and Sec are 248.32, 121.16, and 169, respectively. According to the results (Fig. 3A-**3C**), there were two new species with *m/z* at 372.7 and 418.9, which are considered as the formation of MCL-Cys and MCL-Sec adducts, indicating MCL may modify both the Sec and Cys residues of TrxR. As for the complex between the TrxR USec498 mutant (Sec mutated to Cys form), an obvious specie with *m/z* at 371.1 was detected, indicating that the MCL-Cys adduct was also formed. According to the complex between another TrxR mutant (Truncated form), there was a new specie with *m/z* at 371.1, indicating that MCL-Cys adduct was formed. Taken together, MCL could form the covalent bonds with Cys and Sec.

To further investigate intracellular TrxR, the TrxR green probe assay was performed to assess the intracellular TrxR activity. A specific TrxR fluorescence probe was reported in a previous research [22]. As shown in Fig. 4A and B, the fluorescence intensity was decreased in a dose-dependent manner after treatment with MCL in two HCC cell lines for 24 h (Figs. S3A and S3B). Subsequently, TrxR expression appeared to be degraded with MCL concentrations or in a time-dependent manner (30 μM) for 24 h (Figs. S3C–S3F). According to the intracellular enzyme results, MCL exhibited more inhibition against the TrxR activity than GR activity in the two HCC cell lines (Fig. 4C and D).

TrxR, an intracellular enzymatic antioxidant, plays a critical role in the catalysis of the NADPH-dependent reduction of disulfide in the Trx system, which regulates the cellular redox balance. The inhibition of TrxR disrupts the intracellular redox balance and induces oxidative stress. The ROS generation and cell viability were determined after knocking down the expression of TrxR. Knockdown of TrxR in HCC cells was verified through the Western blot assays (Figs. S3G and S3H). As shown in Fig. 4E-**4H**, MCL displayed more increased ROS generation compared to the cells transfected with the negative siRNA and intact HCC cells. We also investigated the ROS level above through flow cytometric analysis (Figs. S3I and S3J). To further demonstrate whether the down expression of TrxR was involved in the growth of HCC cells, survival analysis was performed, and the results showed that the arrest

Table 1
Inhibition of screened potent compounds on both TrxR and USec498 mutant.

	Score (kcal/mol)	Isolated TrxR (Inhibition %)	Isolated TrxR (USec498)
1. Sinomenine hydrochloride	−9.16	1.20	–
2. Arecoline Hydrobromide	−9.91	/	/
3. Pseudolaric acid B	−9.19	/	/
4. Isoliquiritigenin	−7.33	76.90	–
5. Isoalantolactone	−9.01	79.67	–
6. Glycyrrhetnic acid	−9.72	/	/
7. Micheliolide	−9.87	96.86	–
8. Chelerythrine	−8.17	/	/
9. Dehydrocorydaline	−7.12	/	/
10. Nitidine chloride	−8.11	/	/

"/" presents no activity; "-" presents non-reactive.

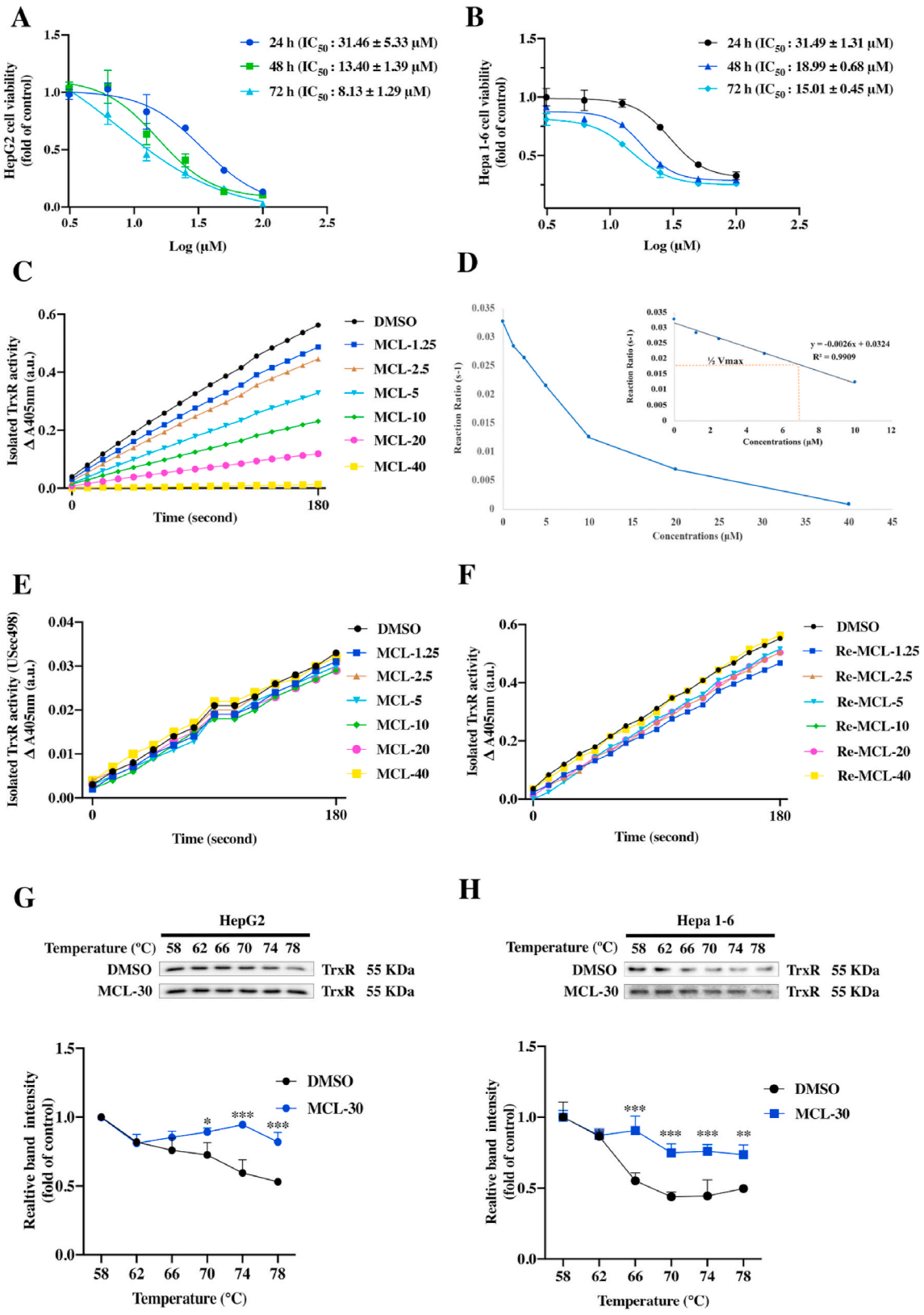

Fig. 2. MCL inhibits the TrxR activity and the growth of two HCC cells. (A) and (B) Analysis of cell viability using CCK-8 following in a time-dependent manner. Each panel shows the HCC cells (HepG2 and Hepa 1–6) were treated with MCL for 24 h, 48 h and 72 h. (C) The TrxR activity was tested through the DTNB monitoring through UV absorption. (D) The kinetic curve of TrxR inhibition by MCL. (E) The Sec depletion mutant of TrxR activity was evaluated in a concentration-dependent manner following the DTNB assay. (F) The pharmacophore of MCL (α-methylene-γ-lactone) was reduced, the new compound named Re-MCL was synthesized, and the Re-MCL against TrxR activity was tested. (G) and (H) The binding affinity of MCL with intracellular TrxR was assessed by the CETSA assays in HepG2 and Hepa 1–6 cells. The TrxR expression was tested by the Western blots. Statistics of grey intensity was normalized in different temperatures. n = 3; ns > 0.05; *, P < 0.05; **P < 0.01; ***, P < 0.001 when compared with control group.

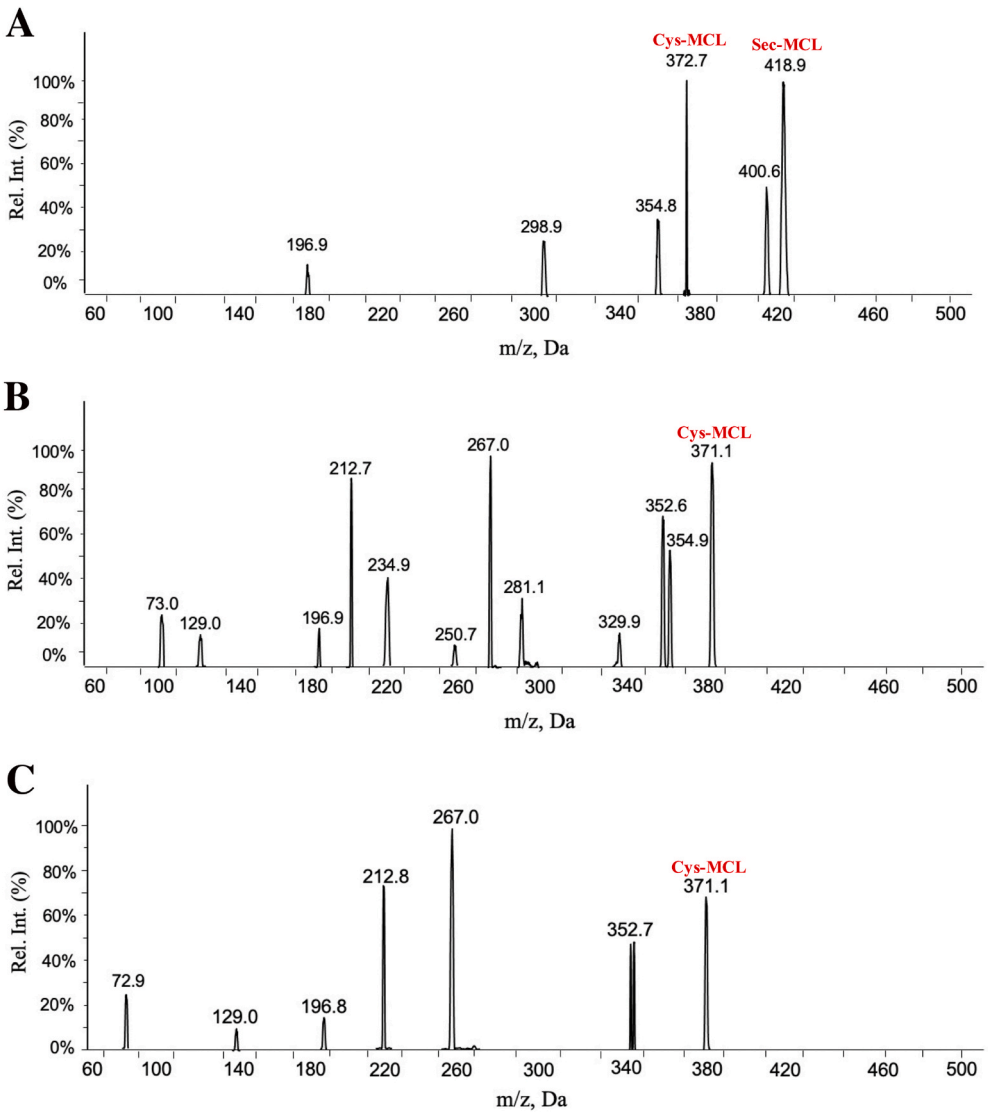

Fig. 3. MCL covalently binds with Sec and Cys of TrxR. (A) MCL was incubated with wild type TrxR, and the adducts were analyzed by the MS. The adduct with *m/z* (372.7) was Cys-MCL; and the adduct with *m/z* (418.9) was Sec-MCL. (B) and (C) MCL was incubated with two TrxR mutants (USec498 TrxR and Truncated form of TrxR), two adducts with *m/z* (371.1) were Cys-MCL of USec498 TrxR and Truncated form of TrxR, respectively.

mechanism of cell growth was due to the knockdown of TrxR (Figs. S3K and S3L). As depicted in Fig. 4I and J, MCL showed significantly higher toxicity against TrxR-downregulated HCC cells compared to the other two groups.

4.3. MCL selectively inhibits TrxR to trigger ROS generation and reduce HCC cell viability

The high reactivity of Sec in TrxR and its accessible location make TrxR enzymes emerge as targets for pharmaceutic drugs. It is well known that TrxR is overexpressed in cancer cells. To gain deeper insight into the comparison between HCC cells and normal liver cells, the identification assays were further performed. As shown in Fig. 5A and B, the TrxR was truly over-expressed in two HCC cell lines compared to the normal cell line (LO_2). After the MCL treatment for 24 h, we found MCL could selectively reduce the viability of HCC cells, indicating the crucial role of TrxR. As shown in Fig. 6A and E, MCL treatment for 24 h dose-dependently induced early and total apoptosis in two HCC cell lines (Fig. 6D and H). In addition, we found that the apoptosis triggered by MCL was completely reversed by the pretreatment (1 h) with NAC (4 mM). NAC possesses the antioxidant ability, which regulates the intracellular redox state. The apoptosis results accounted for that the pretreatment of NAC (the major ROS scavenger) completely neutralized the cytotoxicity of HCC cells with high ROS enrichment, suggesting that oxidative stress is the major regulator of MCL-induced cell death. The apoptosis body assay also shared the same results as the apoptosis analysis (the arrows depict apoptotic bodies) (Fig. S4). Analysis of proteins related to the apoptosis (Fig. 6B and C; Fig. 6F and G) showed that apoptosis inducing factor (AIF) (cytosolic level) and Cytochrome C (cytosolic level) were increased after exposure to MCL. Both modulator proteins play significant roles in initiating the intrinsic apoptosis pathway (early state of apoptosis), which enters into the nucleus to trigger caspase-independent apoptosis. Subsequently, the active caspase9 (Cleaved-caspase9) was found to be activated after the MCL intervention. These results indicated that MCL could induce apoptosis of HCC cells by activating both caspase-independent and caspase-dependent signaling pathways. Importantly, NAC pretreatment could highly prevent these changes.

To further confirm this observation, the ROS levels were subsequently determined in two HCC cell lines after MCL treatment. The DCFH-DA probe was used to detect the ROS generation. As shown in Fig. 7A and B, DCFH-DA staining indicated the ROS occurrence after the

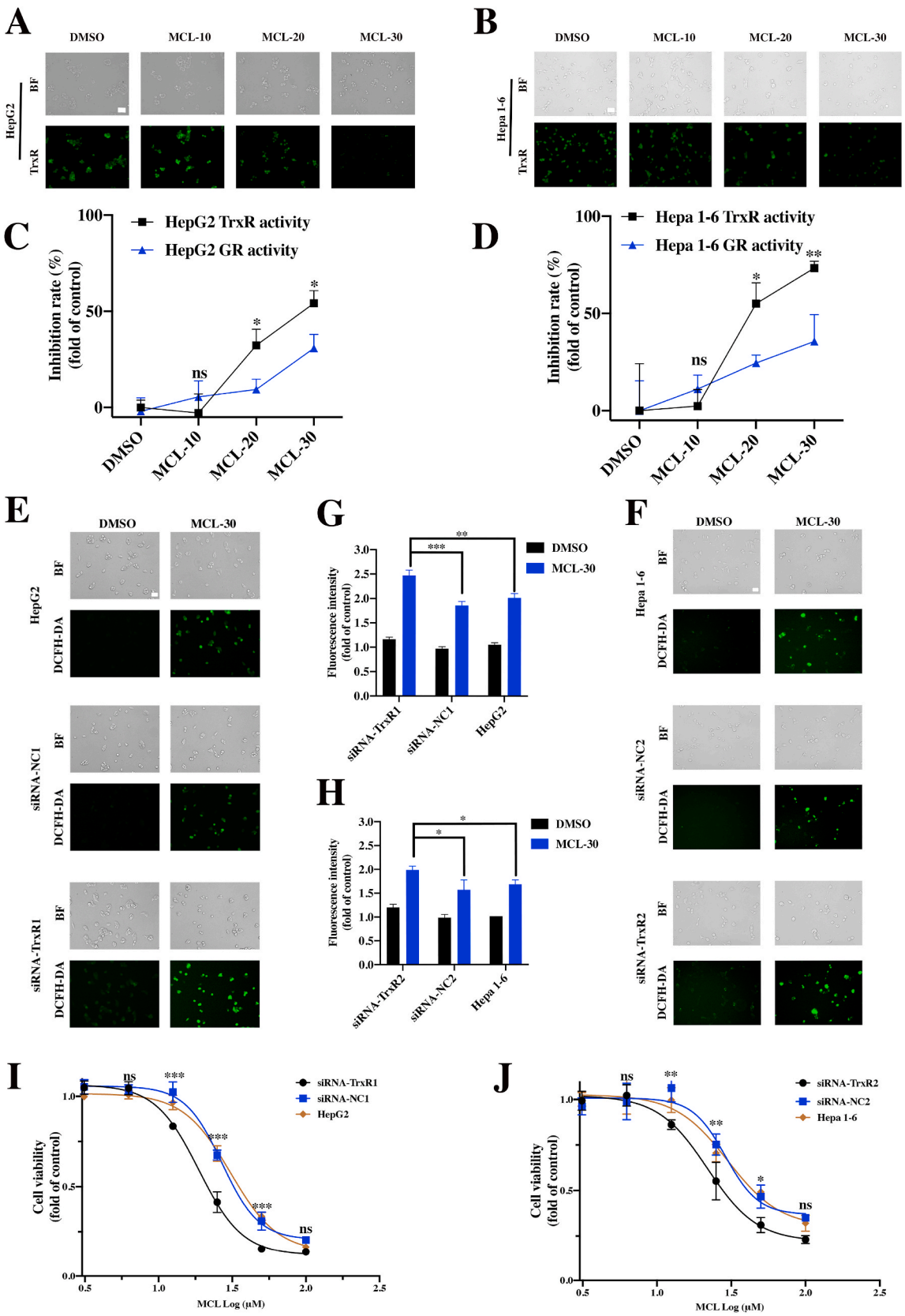

Fig. 4. MCL inhibits the TrxR in two HCC cells (HepG2 and Hepa 1–6) and triggers the ROS generation. (A) and (B) After the treatment of cells with MCL in a concentration manner for 24 h, the TrxR was detected by the TrxR green-probe. (C) and (D) MCL could inhibit the intracellular TrxR in HepG2 and Hepa 1–6 cells after the exposure of 24 h. (E) and (F) ROS generation (DCFH-DA staining) of MCL toward HCC cells, control knockdown cells and TrxR knockdown cells. These cells were treated with MCL (30 μM) (Scale bars: 50 μm). (G) and (H) The fluorescence intensity of ROS level was subsequently analyzed. (I) and (J) Growth inhibition in HCC cells, control knockdown cells and TrxR knockdown cells. These cells were treated with MCL for 24 h n = 3; *, $P < 0.05$; **, $P < 0.01$; ***, $P < 0.001$ when compared with control group. (For interpretation of the references to colour in this figure legend, the reader is referred to the Web version of this article.)

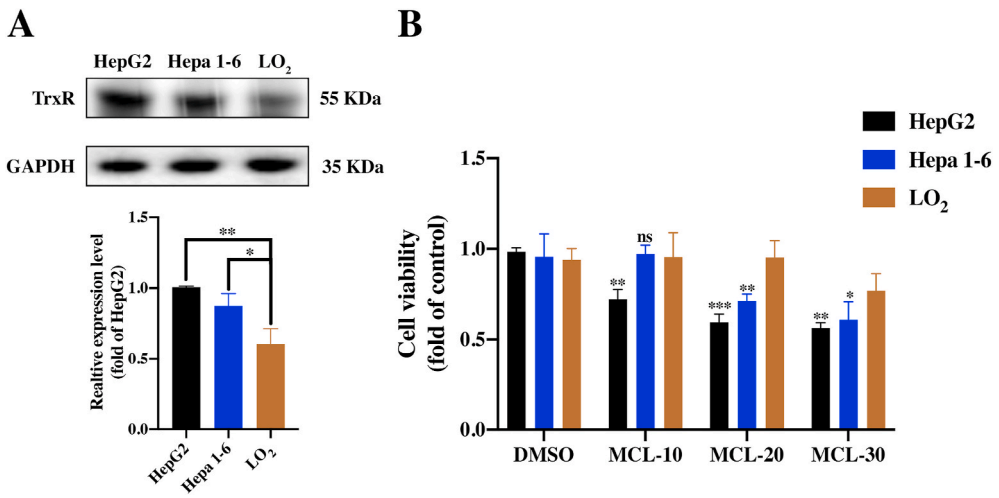

Fig. 5. MCL selectively reduces the viability of HCC cells. (A) The TrxR expression was analyzed in three cell lines. (B) The viability of three cell lines was investigated after MCL treatment for 24 h n = 3; **, P < 0.01; ***, P < 0.001 when compared with the LO_2 group.

cells were stimulated by MCL in a dose-dependent manner, in which MCL (30 μM) triggered a burst of ROS compared to other groups. The flow cytometry presented the same results as the observation of immunofluorescence (Fig. 7C-**7F**). Furthermore, we also pretreated the cells with NAC, which blocked ROS accumulation.

4.4. MCL induces H_2O_2 generation in different organelles

It is known that endogenous oxidants play an important role in the process of tumorigenesis. H_2O_2 performs as the major redox signaling agent and engages in several signaling pathways related to the cellular environment and stress. We monitored the H_2O_2 generation in different organelles after exposure to the MCL for 3 h in two HCC cell lines. HepG2 and Hepa 1–6 cells were implanted with Hyper expression, a generally encoded H_2O_2 sensor protein, which could help monitor the cellular H_2O_2. Each hypervariant targets one of five different sites (cytosol, nucleus, peroxisome, mitochondria, and the ER membrane). To accurately characterize the H_2O_2 generation in different variants, the cell response was recorded and analyzed by the immunofluorescence (Fig. 8A: left panel, HepG2; right panel, Hepa 1–6) and flow cytometry (Fig. 8B). Compared to the control group (Fig. 8C and D), the fluorescence ratio of the mitochondria and nuclear Hyper variants changed significantly, which showed approx. 1.8-fold H_2O_2 generation. For the Hyper located in the ER membrane, the generation had the next highest value, approx. 1.4-fold in all variants. On the other hand, the sites (peroxisome and cytosol) showed similar H_2O_2 response after the exposure to MCL when compared to the control group, which indicated the adjuvant oxidative stress role of the localizations. All the variants of HCC cells were also incubated with 20 μM H_2O_2 for 10 min (Fig. S7), which demonstrated a favorable stability and sensitivity of the Hyper variants model.

4.5. ERS is stimulated by MCL and contributes to ROS-mediated cell death

Previous studies have suggested that the ROS surge is part of pathways of the ERS response, and ROS triggers ERS as a major site of intracellular redox homeostasis. The ER is another organelle that acts as a source of proapoptotic signals [39]. Integration of the mechanisms of apoptosis induced by ERS and ROS is always observed [40]. As shown in Fig. 9A, ultrastructural changes in the ER in HepG2 cells were visualized under TEM. Compared to the negative control group, swollen or enlarged ER lumens were observed after MCL treatment, which presented direct morphological evidence of ERS. Importantly, the morphological changes in the ER were totally normalized after pretreatment with NAC, which suggested that ROS generation induced by MCL played a key role in ERS. On the basis of the above observations, we investigated some ER markers by Western blot assays. The unfolded protein response initiates ERS by transferring eukaryotic initiation factor-2α (eIF2α) into phosphorylated-eIF2α. Transcription Factor 4 (ATF4) is subsequently activated. As a key transcription factor in the ERS, ATF4 transmits the stress signal to the cell death transcription Factor C/EBP-homologous protein (Chop). Additionally, Grp78 and Calnexin are ER chaperone proteins that function as monitors of the ER state. The ERS related markers in HCC cells were measured after MCL treatment. Based on the experimental results (Fig. 9B and E), increased protein expression of Calnexin, Grp78, ATF-4, phosphorylated eIF2α and Chop was observed in response to MCL treatment in both dose- and time-dependent manners (Fig. 9C and F). This was attributed to an initial pretreatment with NAC, scavenging the ROS generated by TrxR inhibition, while the increase in the above proteins was reserved. It is likely that the TrxR inhibitor MCL plays a significant role in ROS-mediated ERS. We subsequently knocked down the expression of TrxR, and then exposure the cells to MCL. TrxR silencing in HepG2 cells increased the expression of the ERS related markers compared to the single MCL delivery alone group (Fig. 9D and G). This is also true for the results in the Hepa 1–6 cell line (Fig. S5).

4.6. MCL induces DAMPs and immunogenic cell death in HCC cells

As has been reported previously, activation of caspase-dependent apoptosis elicits ICD, but caspase-signaling activation is not sufficient to elicit ICD [41]. Herein, specific inducing factors combined with caspase activation in the treatment of malignant cells must cooperate to elicit an antitumor immune response. We have demonstrated that MCL can induce HCC cells through caspase-independent and caspase-dependent signaling pathways. Simultaneously, the ROS generation was observed after exposure to MCL, and ERS was subsequently investigated. As shown in Fig. 10, ERS and the generation of ROS have been shown to contribute to ICD [42,43].

The general markers of ICD include the surface exposure of chaperones, secretion of nucleotides and secretion of endotoxins. Intracellular chaperones such as CRT translocation, and the exposure of HSP 90, sequential secreted ATP and released HMGB1 from the nucleus, are crucial for the immunogenicity of dying or stressed cancer cells. These specific markers toward the surface or the extracellular region of cancer cells prompt regimens of DAMPs, which further present key signals to recruit the immune activation (DCs activation).

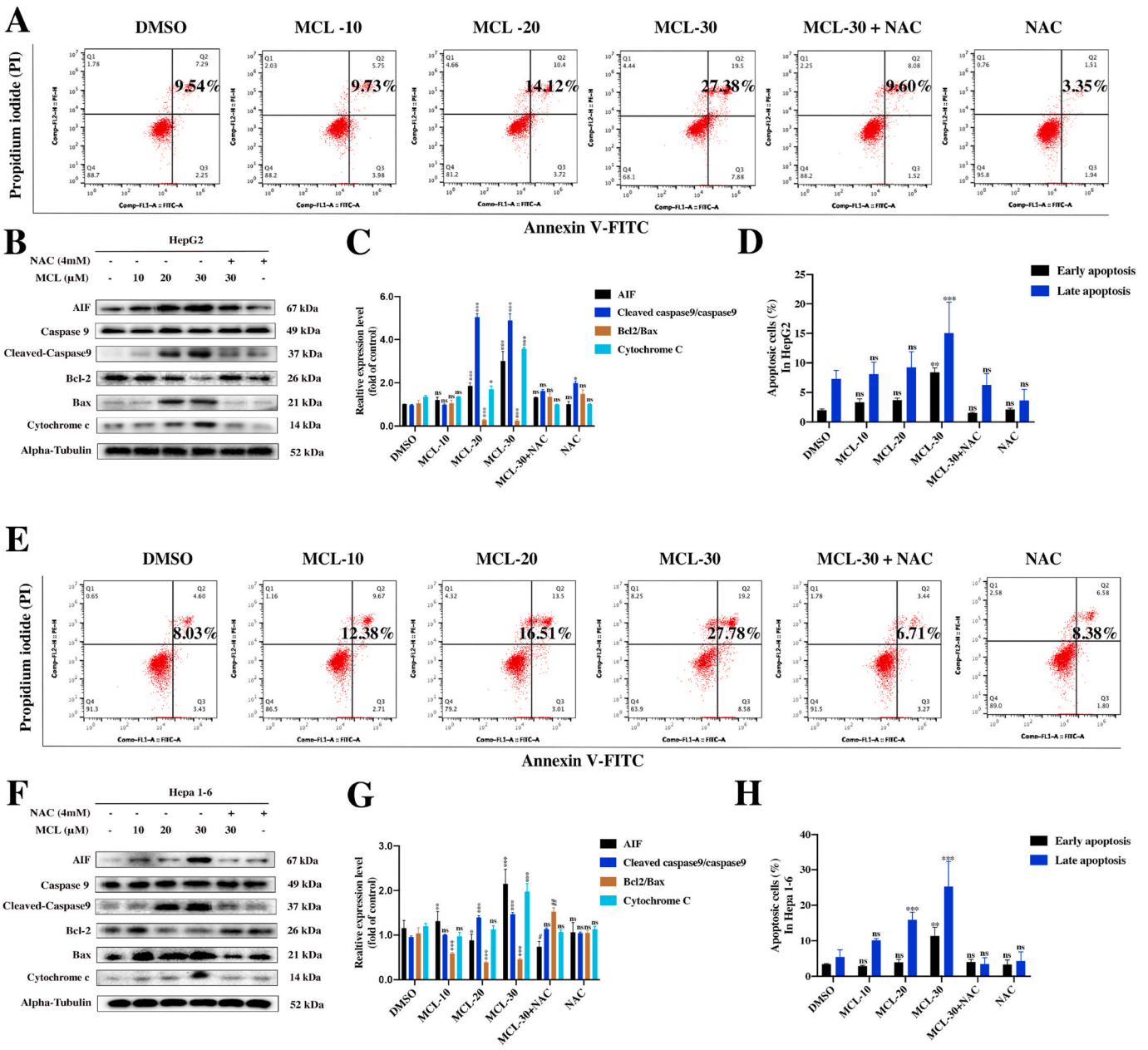

Fig. 6. MCL ROS-dependently induces apoptosis effects of two HCC cells. (A) and (E) HepG2 and Hepa 1–6 cells were treated with MCL (concentration-dependent) for 24 h followed by the assessment of Annexin V/PI staining. NAC pretreatment was performed at 4 mM for 1 h. (D) and (H) The quantification of cell death rate following Annexin V/PI staining. (B) and (F) The signature proteins of apoptosis in two HCC cells challenged with MCL (concentration-dependent) were analyzed by the Western blot assays. (C) and (G) The quantification of the immunoblots was analyzed. n = 3; ns > 0.05; * or $^{\#}$, P < 0.05; ** or $^{\#\#}$, P < 0.01; ***, P < 0.001 when compared with control group.

To further investigate whether MCL exerts the ability to regulate ICD-related markers, corresponding experiments were performed. CRT exposure on the cell surface, delivers the "eat me" signal to the immune system, which stimulates DCs maturation. As shown in Fig. 11A, compared to the control group, increased CRT expression on the surface of the two HCC cell lines was observed after the 24 h of MCL treatment (Fig. S6F). Additionally, CRT expression was further investigated by flow cytometry analyses (Fig. 11C and D). It is insufficient on CRT's own to drive the ICD. HMGB1 ("present me") and ATP release ("find me") were subsequently tested, and compared between the control and MCL treatment groups. Significant HMGB1 release was observed after exposure to MCL, as shown in Fig. 11B, E and 11F. Quantitative analysis of secreted ATP showed that MCL treatment caused obvious ATP secretion in both concentration- and time-dependent manners (Fig. 12D and E), and the NAC pretreatment reversed the ATP secretion effects of MCL. HSP 70/90 is also crucial for the immunogenicity of dying cancer cells. Moreover, an increased level of HSP 90 was also detected (Figs. S6C and S6F). As shown in Fig. 11K-**11N**, the expression of DAMPs (CRT in the membrane, and the HSP 90, and HMGB1 in the cytoplasm) was analyzed. The HSP 70 was not affected by the MCL treatment (data not shown). Notably, pretreatment with NAC significantly counteracted the DAMPs changes induced by MCL treatment.

To further test whether MCL-induced cell death is immunogenic, the DCs was freshly isolated from the bone marrow of C57BL/6 mice. DCs were prepared and induced to differentiate for 6 days. During differentiation, the immature morphology of DCs was observed. (Fig. 12A). The coincubation assay was subsequently carried out and analyzed in flow cytometry (Fig. 12B and C). Compared to the negative control

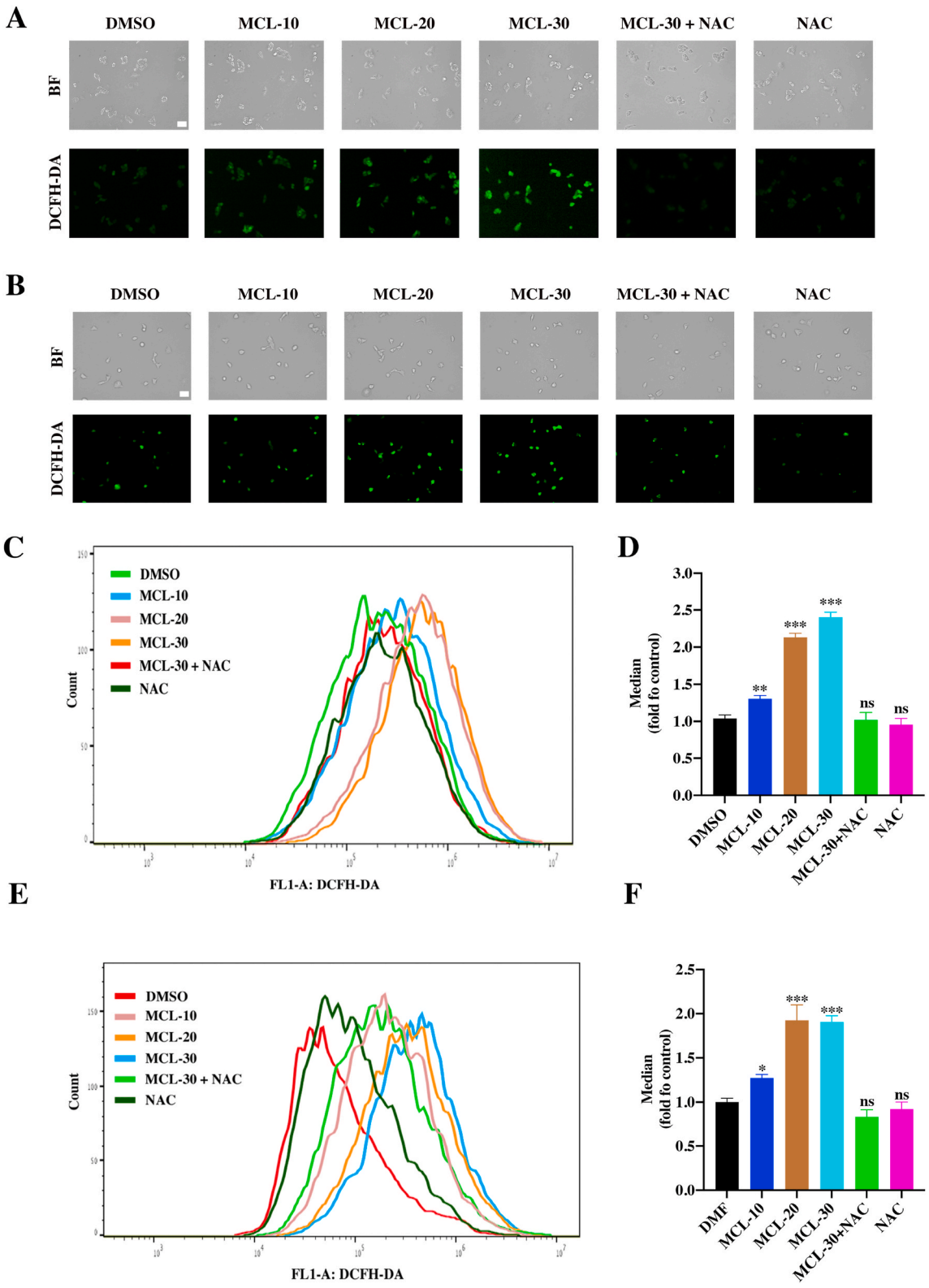

Fig. 7. MCL induces the ROS generation in a concentration-dependent manner. (A) and (B) After the exposure to MCL in two HCC cells (A: HepG2; B: Hepa 1-6), the ROS level was detected by the DCFH-DA probe. NAC pretreatment was performed at 4 mM for 1 h. (C) and (E) The ROS level of each group was analyzed by the flow cytometry, (D) and (F) the median was then calculated and analyzed. n = 3; ns > 0.05; *, P < 0.05; **, P < 0.01; ***, P < 0.001 when compared with control group. Scale bar: 50 μm.

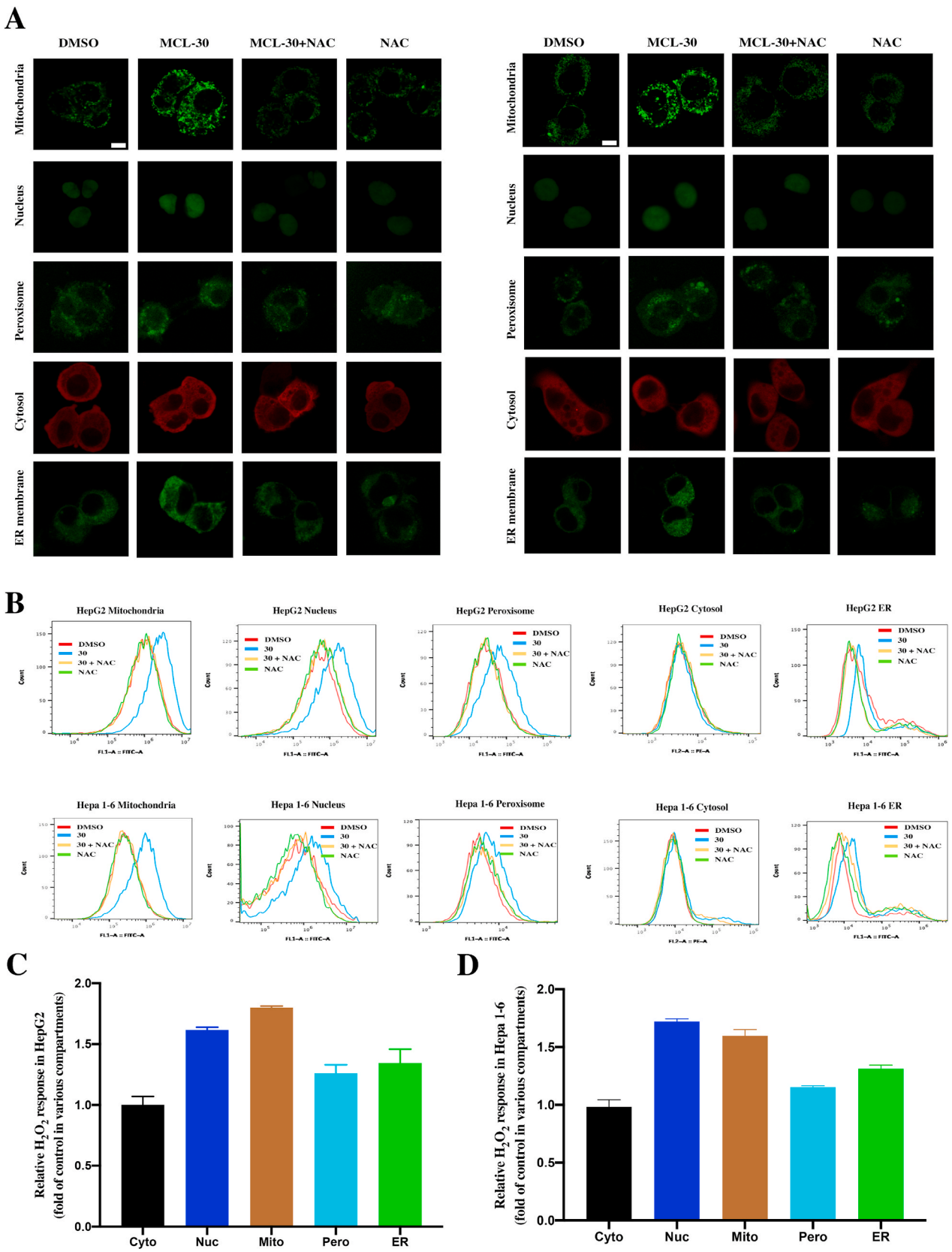

Fig. 8. H_2O_2 generation (HyPer response) in different cell compartments of HepG2 and Hepa 1–6 cells. (A) Imaging of two HCC cells H_2O_2 sensitive HyPer in different cell localizations after the exposure to the MCL (30 μM). NAC pretreatment was performed at 4 mM for 1 h. HyPer response was used to display the location in different cell compartments (mitochondria, nucleus, peroxisome and ER membrane (green); cytosol (red)). (B) The flow cytometry was carried to analyze the HyPer response in different cell localizations. (C) and (D) After the treatment of 30 μM MCL, the relative H_2O_2 response in different localizations of two HCC cells are shown. Data were the results of flow cytometry analysis. Each bar represents the mean of three replicates. Scale bar: 10 μM. (For interpretation of the references to colour in this figure legend, the reader is referred to the Web version of this article.)

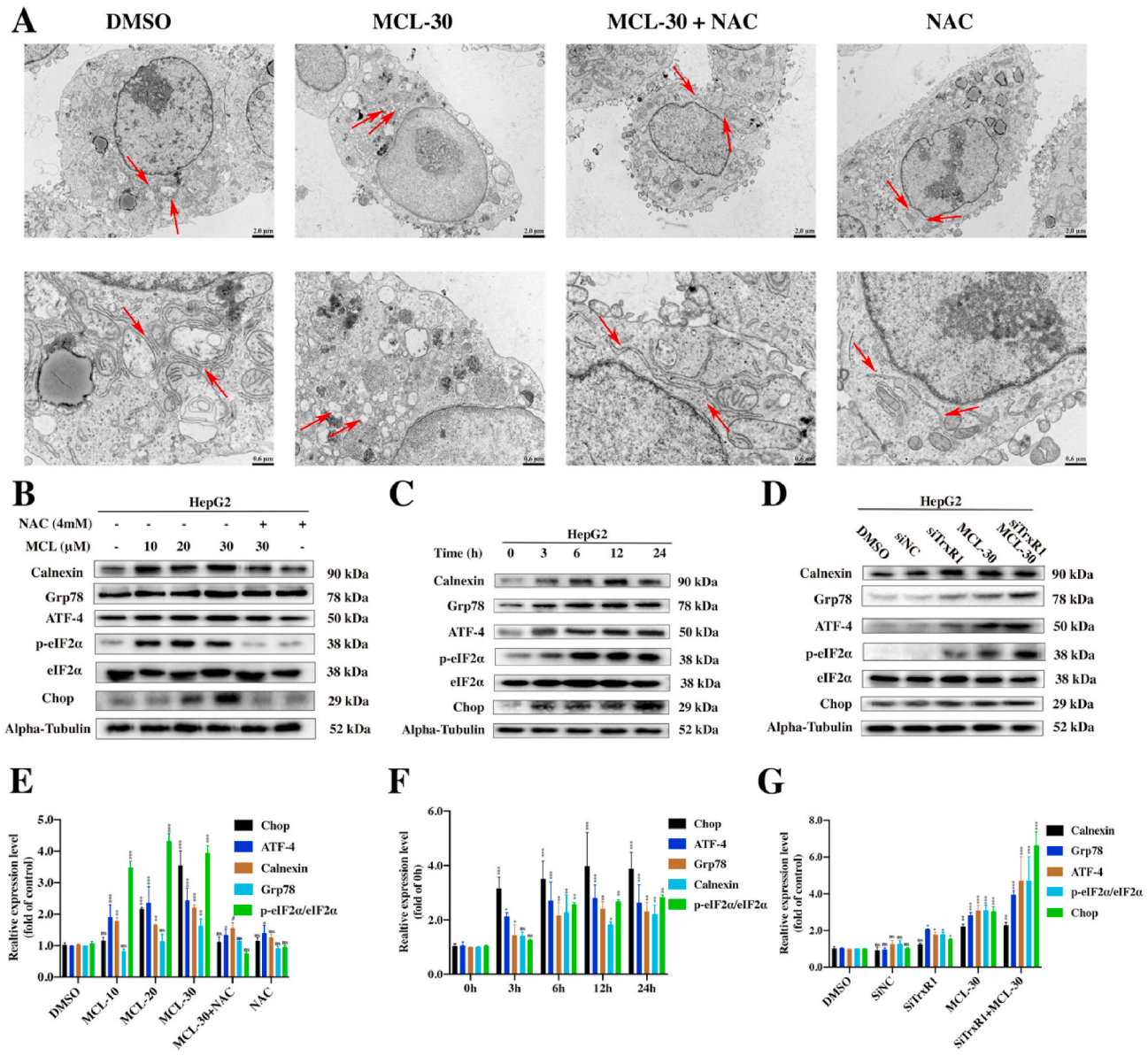

Fig. 9. MCL induces ROS-dependent ERS in HepG2 cells. (A) The images of HepG2 cells exposed to MCL through the electron microscopy, the arrow decorations represent the ER. (B) and (E) ER stress-related proteins of HepG2 cells were analyzed by the Western blot assays. The cells were treated with different concentrations of MCL. NAC pretreatment was performed at 4 mM for 1 h. Densitometric quantification of ERS-related proteins. (C) and (F) ER stress-related proteins of HepG2 cells were by the Western blot assays. The cells were treated with MCL (30 μM) for indicated time points. Densitometric quantification of ERS-related proteins. (D) and (G) The ERS-related proteins were assessed following the transfection of HepG2 cells with siRNA against TrxR before exposed to MCL (30 μM). Densitometric quantification of ERS-related proteins. n = 3; ns > 0.05; *, P < 0.05; **, P < 0.01; ***, P < 0.001 when compared with control group (The Alpha-Tubulin and phospho-eIF2α were used as loading control).

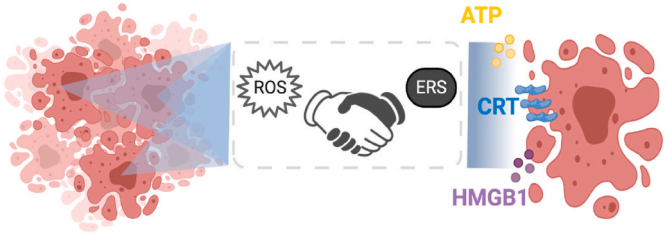

Fig. 10. The prerequisite steps of ICD effects in HCC cells.The figure was created with BioRender.com.

(DMSO group), the treatment with DOX and MCL notably induced DCs maturation. In these, the positive control DOX possessed stronger maturation-inducing effects. Additionally, the MCL induction could be almost entirely counteracted by the pretreatment with NAC.

4.7. MCL exerts anti-HCC vaccination effects in vivo

The initial stimulation of cancer cell death plays a decisive role in the tumor microenvironment. They are generally categorized into immunogenic or nonimmunogenic. Unlike intrinsic cell death, ICD can stimulate the activation of the host immune response and some immunotherapeutic approaches, such as DC-based cancer vaccination [44,45]. To further investigate whether MCL treatment could induce HCC vaccine effects in the intact immune system mice, a tumor rechallenge assay was performed. Seven days after the treated Hepa 1–6

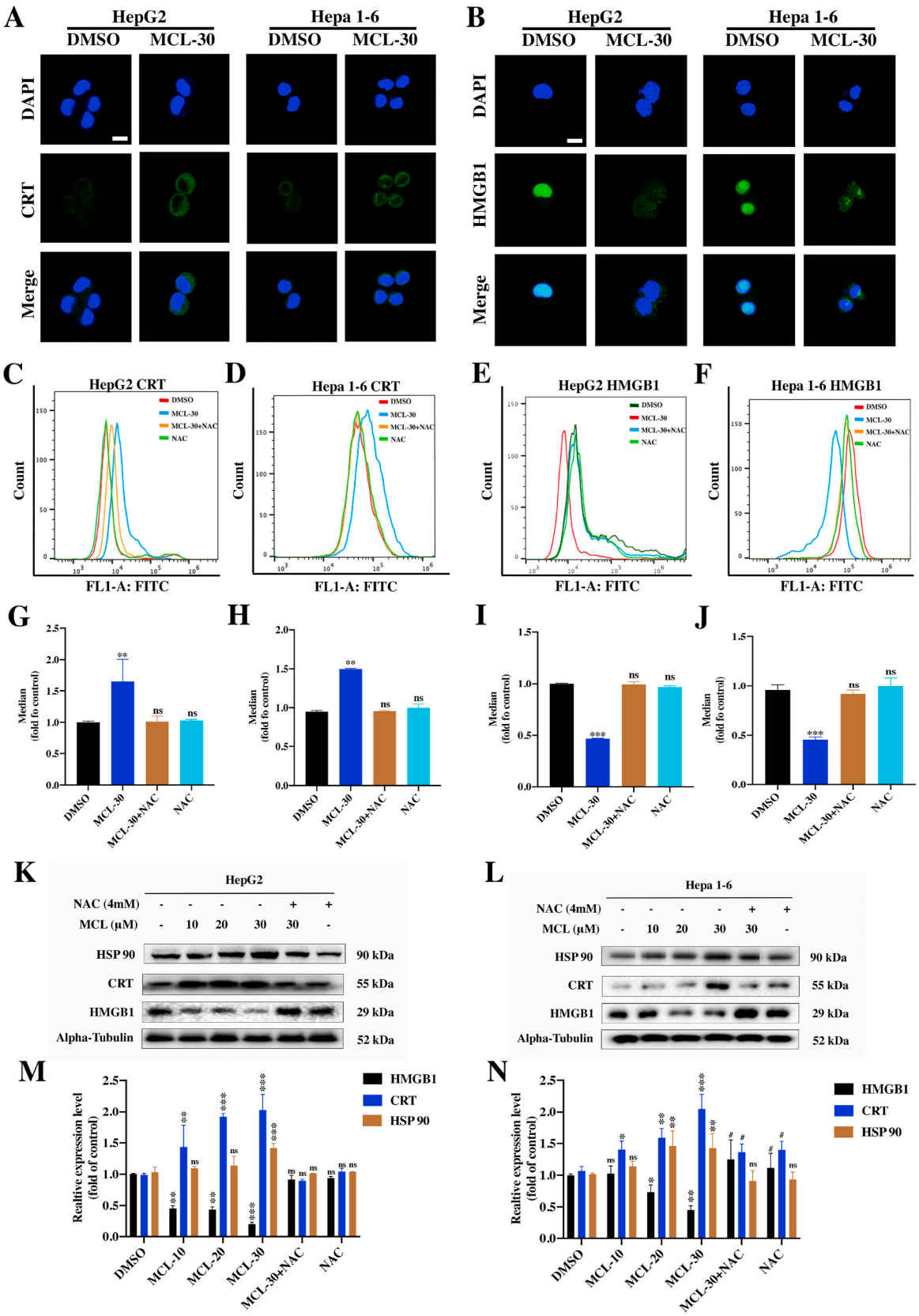

Fig. 11. MCL induces DAMPs of HepG2 and Hepa 1–6 cells. (A) and (B) After the treatment of MCL (30 μM) toward two cells for 24 h, the images of CRT and HMGB1 were detected by the immunofluorescence. (C–F) The flow cytometry analysis of CRT and HMGB1 in two cells following exposed to MCL (30 μM) for 24 h is exhibited. (G–J) The mean of the flow cytometry results was calculated and analyzed. (K) and (L) DAMPs related proteins of HepG2 and Hepa 1–6 cells were analyzed by the Western blot assays. The cells were treated with MCL in different concentrations. NAC pretreatment was performed at 4 mM for 1 h. (M) and (N) Densitometric quantification of proteins (HSP 90, CRT and HMGB1). n = 3; ns > 0.05; * or $^{\#}$, P < 0.05; **, P < 0.01; ***, P < 0.001 when compared with control group (The Alpha-Tubulin was used as loading control). Scale bar: 10 μM.

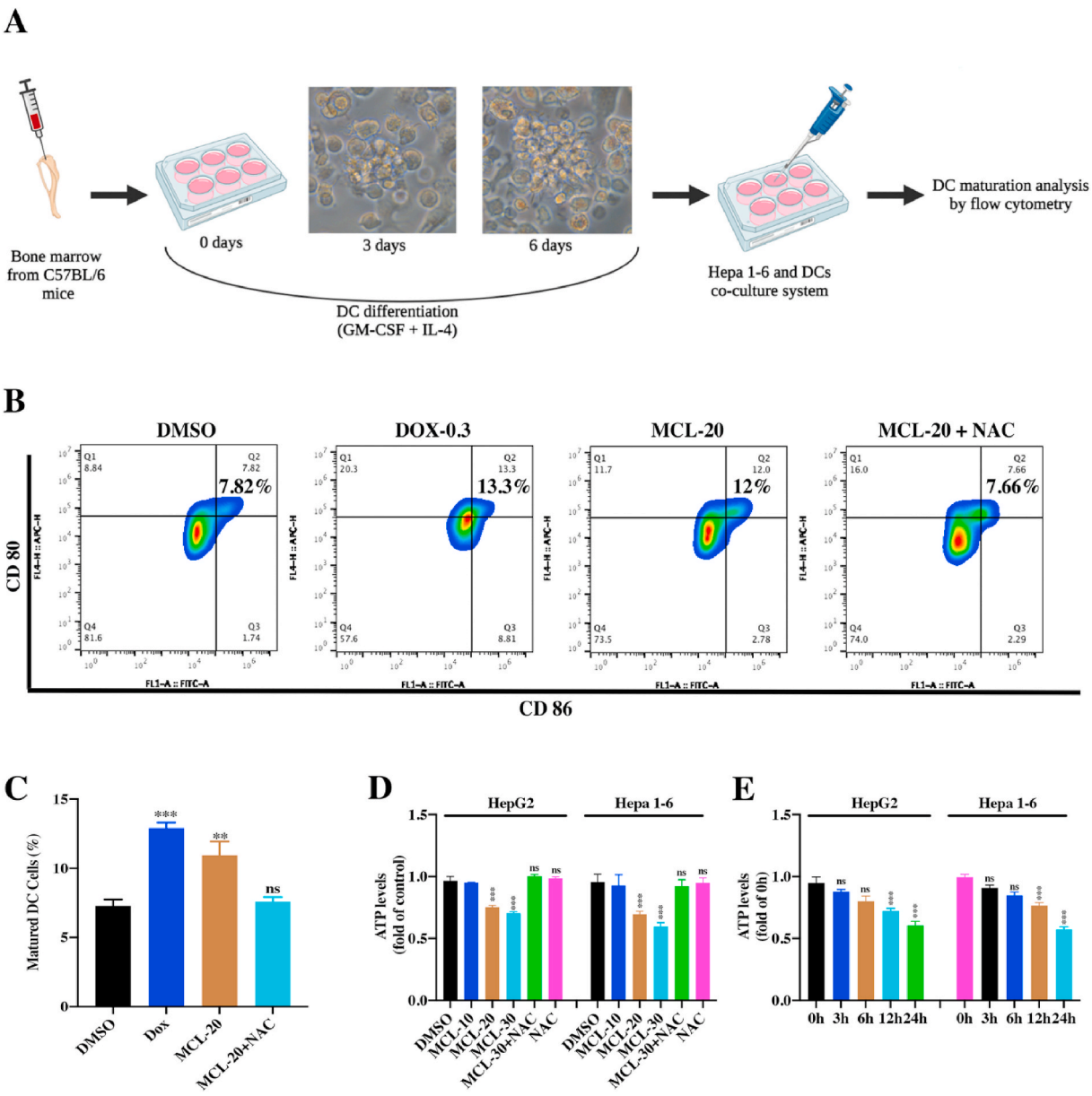

Fig. 12. MCL promotes DCs maturation. (A) The scheme of murine DCs isolation, differentiation, and maturation analysis. 200× magnification. The figure was created with BioRender.com. (B) After the MCL or DOX treatment, the treated Hepa 1–6 cells were then co-cultured with immature DCs for another 24 h. The CD80 and CD86 positive cells were analyzed by the flow cytometry. (C) Quantification of mature DCs following the CD80 and CD86 staining. (D) The intracellular ATP level (HepG2 and Hepa 1–6 cells) was analyzed after MCL treatment in a concentration-dependent manner. (E) After the two HCC cells exposed to the MCL (30 μM) in different time points, the intracellular ATP was analyzed by the ATP ELISA assays. n = 3; ns > 0.05; **, P < 0.01; ***, P < 0.001 when compared with control group.

cells were inoculated on the right armpits of C57BL/6 mice, freshly prepared nontreated Hepa 1–6 cells were inoculated on different sides of the armpits in mice (Fig. 13A). The mice were continuously monitored for 17 days, the tumor growth and incidence were recorded, the renascent tumor size on the left side of each group was not obviously different (Fig. 13C), and the body weights of the mice in the three groups were not significantly changed (Fig. 13D). Strikingly, on Day 7, the number of tumorigenic mice in the PBS-treated group reached almost half of the total. The incidence of tumorigenic mice in both the MCL and DOX treatment groups was lower. Tumors started to appear approximately one week after rechallenging, and 100% incidence was recorded in PBS on Day 17. The tumorigenic incidence of MCL treatment was moderate, and the lower incidence was observed in the positive control DOX treatment (Fig. 13B). According to the characteristic immune response and memory against Hepa 1–6 cells, we conjectured that the Hepa 1–6 cells treated with MCL or DOX can release the ICD markers (DAMPs), which not only stimulate the immune effector cells to kill Hepa 1–6 cells (the right armpits) but also induce a potential immune memory response (the left armpits).

4.8. MCL remodels the tumor immunity to suppress HCC development

To investigate the effect of MCL treatment in vivo, C57BL/6 tumor-bearing mice were designed and challenged. Seven days after the Hepa 1–6 cells inoculation, the mice were randomly divided into the three groups. Then, mice were treated with PBS as the model group, MCL (25 mg/kg) and DOX (1 mg/kg) as the test group and positive control group, respectively. During the continuous monitoring, the MCL treatment impressively mitigated rapid tumor growth compared to PBS group, but the positive control DOX exhibited the best inhibition of tumor growth,

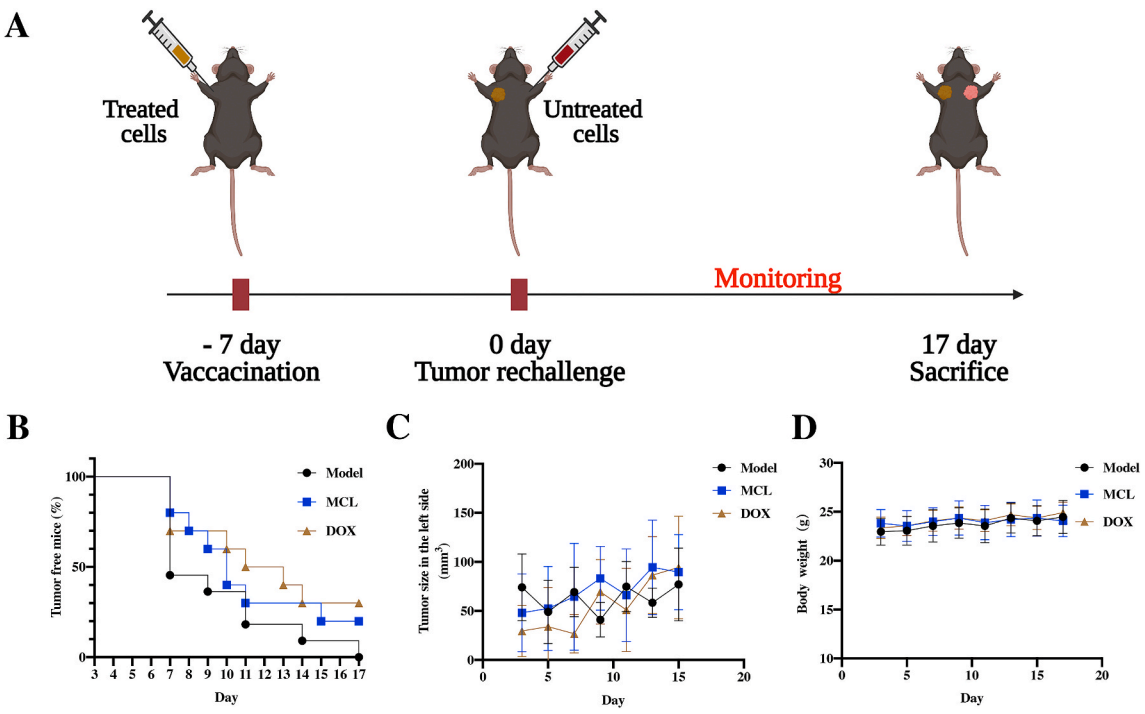

Fig. 13. MCL shows specific immune response (vaccine effects) in advanced HCC suppression. (A) The scheme of tumor incubation and treatment approach. (B) The tumor free curve of Hepa 1–6 tumor on the left side in mice after the different treatments (n = 7). (C) The renascent tumor volume in the left side of each group. (D) The changes of mice body weight.

as shown by tumor growth curves (Fig. 14C). The tumor weight of each group was also analyzed (Fig. 14D). There was no significant change in the weight of each group (Fig. 14E). After the mice were sacrificed, the tumor samples were extracted, and the tumor bulks were weighed and photographed (Fig. 14A). As shown in Fig. 14B, H&E and TUNEL immunofluorescence staining of the tumor tissues in each group was analyzed. To confirm whether MCL induced the ICD by inhibiting the TrxR, ICD markers, TrxR activity and ROS generation were subsequently detected. The TrxR activity in tumors was tested. Compared to that in the PBS group, TrxR expression in the MCL treatment group was significantly decreased, indicating that MCL could suppress the tumor growth by inhibiting the TrxR (Fig. 14F-**14I**). TrxR in the DOX treatment group was also decreased, and we speculated that the TrxR activity was regulated by the comprehensive effects of DOX.

Then, the ROS generation in tumors was detected by immunofluorescence with two probes. As shown in Fig. 14J, the MCL and DOX groups could significantly induce the ROS generation compared with the PBS group. Moreover, the ERS markers were investigated. Except for the chaperone protein Grp78, all the ERS factors were in good agreement with the in vitro results (Fig. 15A and B). ROS generation and ERS are required for the development of ICD. CRT exposure and HSP 90 overexpression with MCL and DOX treatment were observed in tumors (Fig. 15C and D). Compared to the PBS group, HMGB1 was significantly released in both the MCL and DOX groups. To further investigate whether MCL treatment exerted immunoregulatory effects on the HCC model, the frequency of various immune cells in tissues was isolated and examined by flow cytometry. Accordingly, the number of activated DCs in the spleen was upregulated upon the MCL treatment (Fig. 16A). As shown in Fig. 16B and C, other immunosurveillance cells, including $CD8^+$ T cells and $CD4^+$ T cells, were also upregulated after the treatment. In both MCL and DOX treatment, the immunostimulatory cytokines, including IFNγ and TNFα, increased significantly (Fig. 16D and E). To further evaluate the safety of MCL for the potential of HCC therapy, the biosafety-associated toxicological pathology was analyzed. As shown by the hematoxylin and eosin (H&E) staining (Fig. S8), there was no obvious injury to the main organs, including the heart, liver, spleen, lung, and kidney.

It is well acknowledged that the tumor angiogenesis and the tumor microenvironment share a strong correlation. As tumor growth depends on tumor angiogenesis, metronomic chemotherapy has also been shown to irritate the antitumor immune response and inhibit the tumor angiogenesis [46]. It is necessary to evaluate the antiangiogenetic effect of MCL in a dose-dependent manner. A zebrafish model system was used to determine whether MCL treatment could suppress angiogenesis in vivo. It is easy to observe due to the transparency of zebrafish embryos. All the compounds were dissolved in culture medium containing 0.1% DMSO (v/v) and incubated with embryos from a transgenic zebrafish (GFP expression in the endothelium) for 24 h. MCL could inhibit angiogenesis of SIV plexus in a dose-dependent manner, in which a high concentration could cause embryonic lethality (Fig. S9). In addition, at a dosage of 0.5 μM, DOX reduced the angiogenesis of zebrafish embryos.

4.9. Evaluation of the initial clinical utility of MCL treatment

HCC resistance has already emerged. Further evaluation of the MCL-effects in potential HCC clinical treatment is necessary. According to the results of Huh7R cell viability, we found that MCL could significantly inhibit the growth of Huh7R cells as well as nonresistant HCC cells, whose IC_{50} was 14.12 μM at 72 h (Fig. S10D). Due to the crucial role of the pharmacophore (α-methylene-γ-lactone), we further evaluated the inhibition of Re-MCL ($IC_{50} > 100$ μM). The results accounted for the fact that the α-methylene-γ-lactone was the crucial pharmacophore of MCL. The results of the TrxR green-probe assay further corroborated this notion (Figs. S10A and S10B). We also found the ROS generation in Huh7R cells after exposure to MCL, while NAC pretreatment reversed the effects (Figs. S10C and S10E). The organoid model is a real pathological model of target tumor formation, which further identifies the value of drug candidates in the clinic. The HCC organoid model was generated and incubated with different treatments for six days. The number and the size of organoids were analyzed under the microscope every three days (Fig. 17). The positive control groups all inhibited the growth of HCC organoids, as the figure shown in Fig. S11. Excitingly,

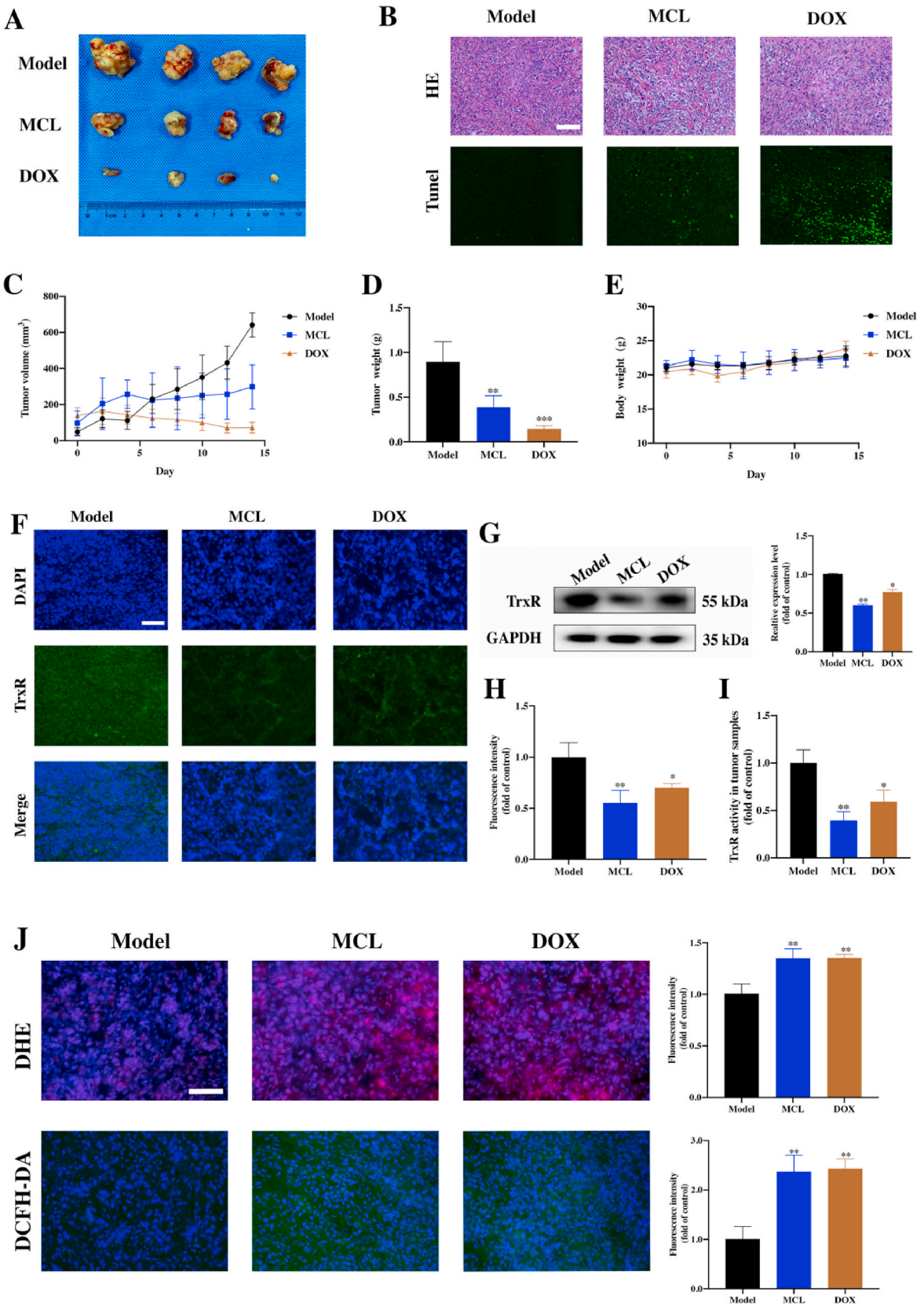

Fig. 14. Therapeutic efficacy of MCL on suppressing cells in Hepa 1–6 tumor-bearing C57BL/6 mouse model. (A) Representative photographs of dissected tumors of each group. (B) H&E and TUNEL immunofluorescence staining of the tumor tissues in each group. Scale bar: 100 μm. (C–E) The tumor volume changes; the tumor weight and the body weight of mice were recorded. (F) and (H) The TrxR immunofluorescence stainings of tumor tissues after various treatments were analyzed. Scale bar: 100 μm. (G) The Western blot analysis of TrxR expression in tumor tissues of each group. (I) The TrxR activity of tumor tissues in three groups were analyzed. (J) The DHE and DCFH-DA immunofluorescence staining of tumor tissues and fluorescence intensity were detected and analyzed. Scale bar: 100 μm n = 4; ns > 0.05; *, P < 0.05; **, P < 0.01; ***, P < 0.001 when compared with model group.

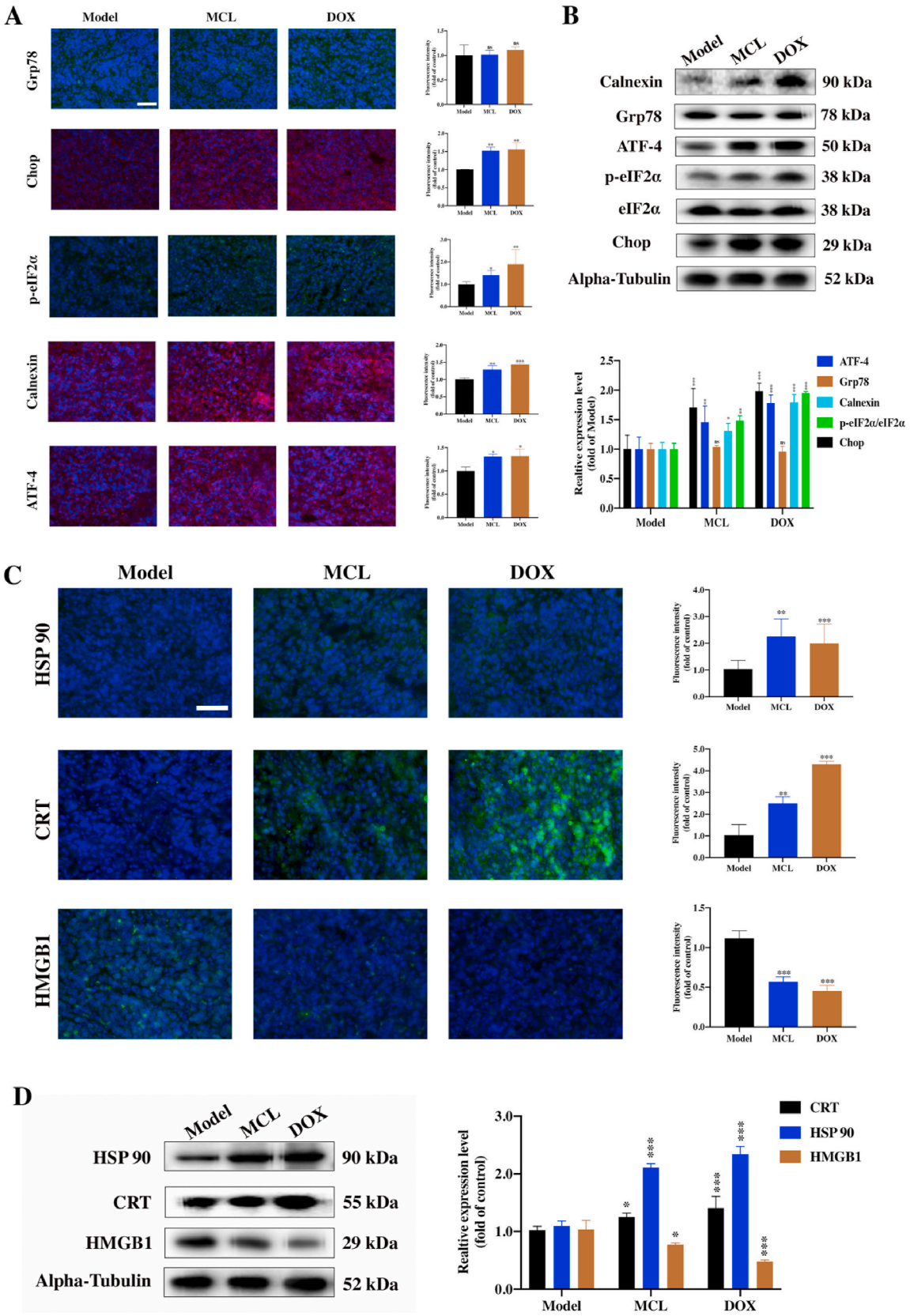

Fig. 15. MCL elicits ERS and induces DAMPs (ICD-related markers) in vivo. (A) The proteins (Grp78, Calnexin, ATF-4, p-eIF2α and Chop) immunofluorescence staining of the tumor tissues. Scale bar: 100 μm. (B) The ERS associated proteins of tumor tissues were analyzed by the Western blot assay. Densitometric quantification of ERS-related proteins. (C) The DAMPs (HSP 90, CRT and HMGB1) immunofluorescence staining of the tumor tissues. Scale bar: 100 μm. (D) The Western blot assays were carried out to assess the DAMPs expression of tumor tissues of each group. n = 4; *, $P < 0.05$; **, $P < 0.01$; ***, $P < 0.001$ when compared with model group.

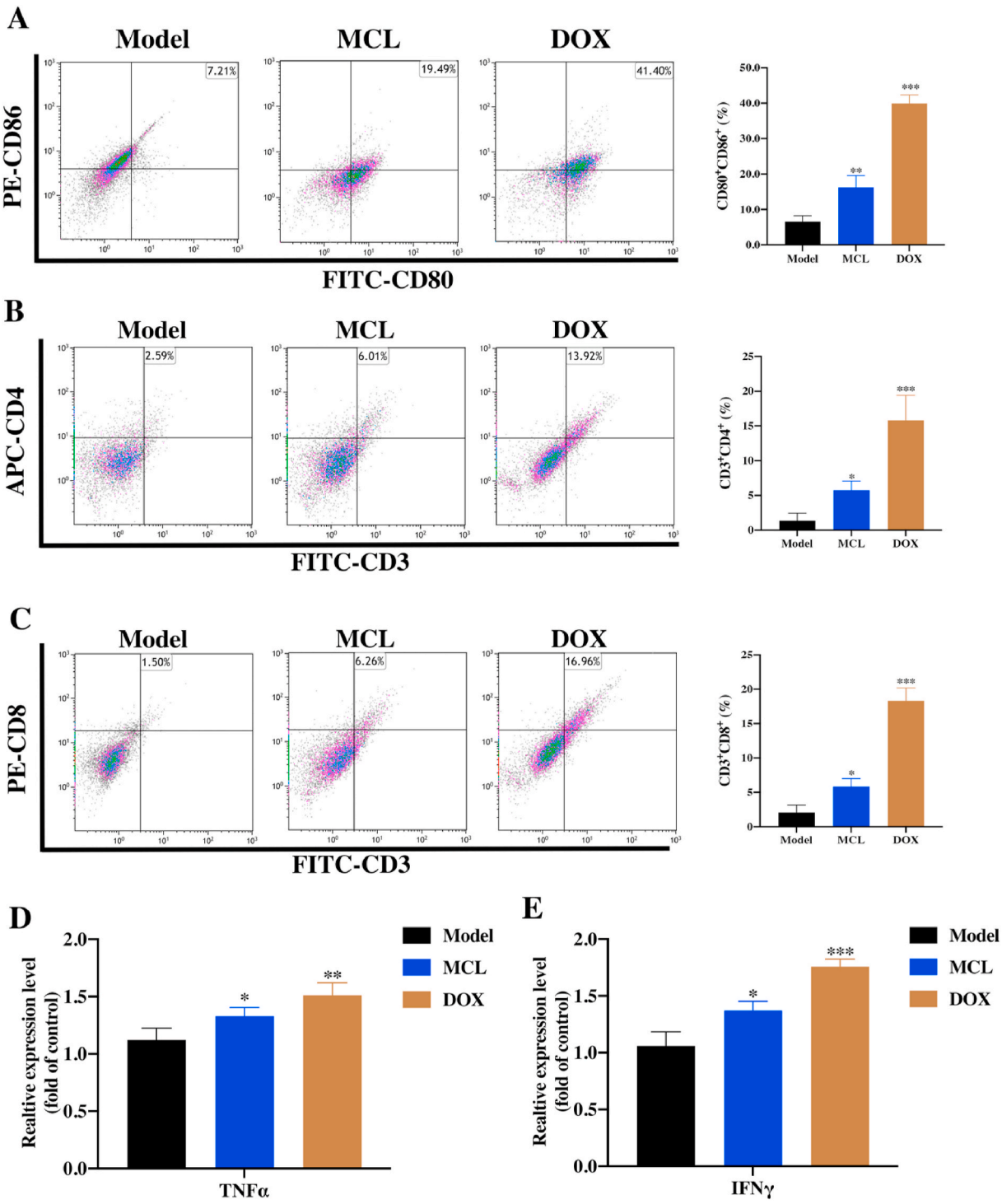

Fig. 16. MCL remodels immune response of Hepa 1–6 tumor-bearing C57BL/6 mice.
(A) The flow cytometric examination of mature DCs (gated on $CD80^+$ and $CD86^+$ cells) of spleen tissues. (B) and (C) The CD4 T cells (gated on $CD4^+$ and $CD3^+$ cells) and the CD8 T cell infiltration (gated on $CD8^+$ and $CD3^+$ cells) in tumor tissues were analyzed by the flow cytometry. (D) and (E) The proinflammatory cytokines including TNF-α and IFN-γ in the serum were analyzed by the ELISA assays. n = 4; *, $P < 0.05$; **, $P < 0.01$; ***, $P < 0.001$ when compared with model group.

MCL exhibited great antiproliferative activity in a concentration-dependent manner. Consequently, MCL treatment against HCC exhibited great initial clinical utility.

5. Discussion

The common intervention for the treatment of primary liver cancer and metastatic liver cancer is the liver resection. After the surgery, systematic chemotherapy or localized and targeted chemotherapies are commonly applied. Most traditional chemotherapy drugs are designed to block the growth of cancer cells by acting with specific targets and inducing the process of cell death. Unfortunately, cancer cells have developed new escape mechanisms to circumvent the antitumor effects of existing drugs, which may lead to present off-target effects and form a resistant tumor accompanying tumor progression. Searching promising anticancer targets and discovering their potential inhibitors or inducers

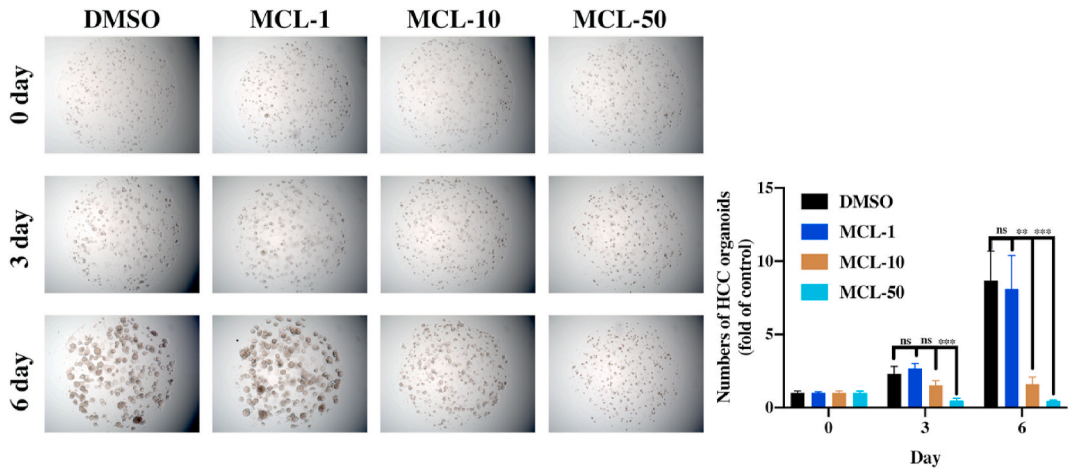

Fig. 17. MCL significantly inhibits the growth of HCC organoids (50 ×). n = 3; ns > 0.05; **P < 0.01; ***, P < 0.001 when compared with control group.

may be an ideal approach for future cancer therapy. Recently, the potential rewiring redox state has been regarded as one of tumor resistance mechanisms [47]. Due to vigorous cell metabolism and proliferation, the interest in the ROS-inducing therapies in the cancer treatment has emerged. Excessive ROS in the process of redox homeostasis could be limited by scavenged balance systems, which include the thioredoxin system. TrxR reduces the oxidized substrate Trx with electrons from the NADPH assistant [12]. The inhibition of TrxR could elicit ROS generation and induce cancer cell apoptosis. The existing TrxR inhibitors fall into two categories (natural products and gold complexes). Most of them have been reported to induce this form of programmed cell death, which focuses primarily on the tumor cells themselves [14,48,49]. Only a few studies have mentioned the association between the TrxR inhibitors and the tumor microenvironment (TME). Recently, the gold complex auranofin (a classical TrxR inhibitor), has been proven to trigger the innate immunity in mutant p53 non-small-cell lung cancer [50]. The codelivery system consisting of curcumin could ameliorate the immunosuppressive microenvironment to inhibit the growth of lung cancer cells [51]. In the present study, we screened out the promising TrxR inhibitor MCL, investigated the reaction between MCL and TrxR, and further analyzed MCL in the H_2O_2 response process in the cell interior. We have also demonstrated that MCL can elicit the ROS-mediated ERS signals to DAMPs to induce ICD in HCC cells (Fig. 18).

Given the diverse resistance mechanisms of HCC cells, the further development of covalent inhibitors could increase the occupation rate of binding sites, which achieves more anticancer efficiency [52]. In our studies, we have provided evidence that MCL can bind with the carbon-terminal residue of Sec 498 of TrxR through the α, β-unsaturated carbonyl. Further CESTA assays also clarified the fact that MCL binding with the TrxR impeded the degradation of the TrxR protein following the condition of temperature variation. According to the results of TrxR (USec498, Sec 498 by a "knockin" of the Cys 498) activity assay, we found that MCL rarely targeted and inhibited the TrxR (USec498). In the complex intracellular environments, MCL exhibited more inhibition against intracellular TrxR than GR. Collectively, MCL showed major inhibitory effects against TrxR.

The close relationship between TrxR and intracellular redox has been demonstrated previously. The changes of TrxR from the reduced state to the oxidized state could trigger a specific term named "SecTRAP" (Sec-compromised TrxR-derived pro-apoptotic protein), which causes an intracellular rapid oxidant environment [53,54,65]. The foreign materials/exposure inducing the intracellular oxidant has a particular

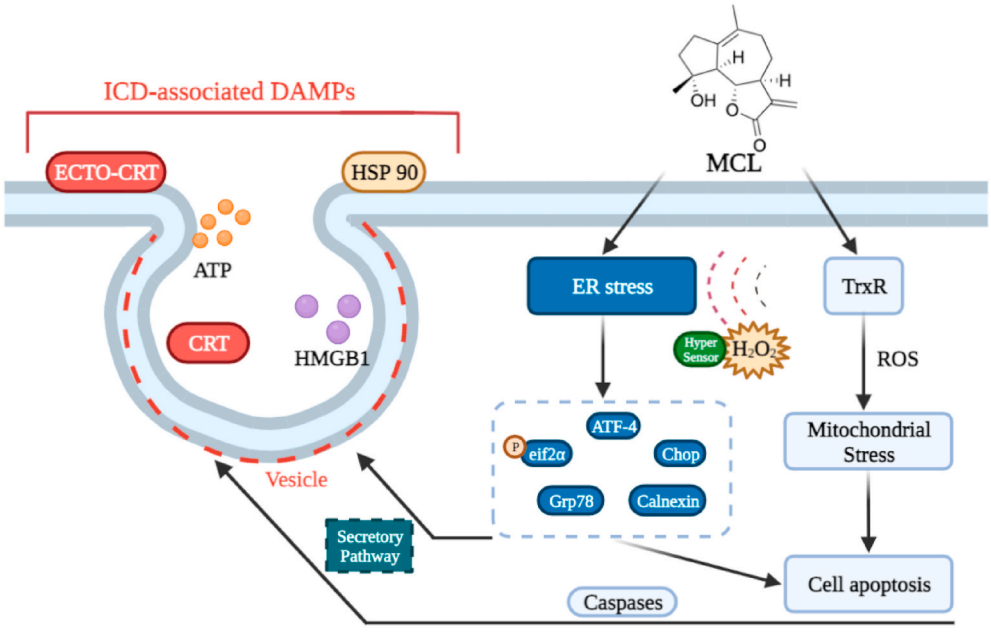

Fig. 18. The schematic illustration of underlying mechanism of ICD effects inducing by MCL. The figure was created with BioRender.com.

designation "exposome", which includes drugs, toxicants and physical stressors [55]. We found that MCL acted as an "exposome" to induce the ROS generation in two HCC cell lines as well as in the tumor-bearing model. Additionally, there is always a feedback regulation of the redox balance mechanism. It has been reported that the NAC or vitamin E can reverse the oxidative stress by disrupting ROS-p53 signals in KRAS-induced lung cancer [56]. According to the results of NAC pre-treatment, NAC presented "reverse" effects to block the ROS_stress consequences of MCL treatment. Due to the variable exposome, it is necessary to determine the contribution of the exposome and the distribution of ROS generation [57].

To determine the topology of H_2O_2 production by MCL, two HCC cell lines expressing five Hyper-sensors were constructed. The mitochondrial H_2O_2 was highly released after the exposure to MCL compared to other intracellular Hyper sensors. Notably, a previous study also proved that MCL could suppress the growth of HCC cells by the aggregation of mitochondria and perturbation of F-actin fibers, and exposure to MCL presented the ROS-mitochondria-apoptosis axis [36].

Interestingly, the ER possesses close contact with mitochondria with fictional consequences. The Ca^{2+} influx plays a critical role in the contact sites between mitochondria and the ER [58]. Our results indicated that Ca^{2+} mobilization from the ER responded to the ERS, and ER-H_2O_2 production was also observed after the MCL exposome (Fig. S6D, **S6E** and **S6G**). The MCL exposome of HCC cells generates intracellular ROS and oxidized stress, which triggers the intracellular "cold state" to transform into "hot state". The hot state of the cellular microenvironment plays a crucial impact on redox signaling, especially the immune response axis. The surge of intracellular ROS and ERS could elicit the DAMPs of cells, which serve as landmarks for ICD. We showed that MCL could induce the ICD in two HCC cell lines and promote the DCs maturation in a coculture model of Hepa 1–6 cells. Furthermore, the tumor vaccine provides strong proof of the immune response to MCL in a mouse model.

Lenvatinib, acting as a multiple kinase inhibitor, is generally used as a promising strategy in the clinic for the treatment of people with unresectable HCC [59]. According to the latest clinical feedback, there are already some HCC patients with lenvatinib resistance [60–62]. It is exciting that MCL could suppress the growth of Huh7-lenvatinib-resistant cells, and the results of further assays demonstrated that MCL could induce the ROS generation in resistant cells by inhibiting the TrxR activity. Interestingly, according to the zebrafish angiogenic assessment model, we found that MCL clearly showed significant antiangiogenic effects. Notably, the HCC organoid results also accounted for some potential clinical implications of MCL, which could decrease the organoid size in concentration-dependent and time-dependent manners.

In conclusion, we successfully screened out the promising TrxR inhibitor MCL and uncovered a potential mechanism of ICD effects induced by MCL (TrxR-ICD axis) in HCC treatment. We further investigated the reaction between MCL and TrxR. We first analyzed the intracellular H_2O_2 production after MCL treatment, and the results showed that MCL induced ROS generation-ERS to elicit the ICD in HCC cells. Remarkably, MCL exhibited vaccine effects in vivo, reduced the growth of HCC xenografts and stimulated the immune response, and further decreased the HCC organoid sizes. Taken together, MCL requires further investigation and is expected to be applied in clinical settings in the future.

Declaration of competing interest

The authors declare that they have no known competing financial interests or personal relationships that could have appeared to influence the work reported in this paper.

Acknowledgments and Funding

We thank the financial supports of the National Natural Science Foundation of China (No. 82173684 and No.81703337), the Open Project of Chinese Materia Medica First-Class Discipline of Nanjing University of Chinese Medicine (No. 2020YLXK010), the Priority Academic Program Development of Jiangsu Higher Education Institutions (Integration of Chinese and Western Medicine), the Jiangsu Province Graduate Practice Innovation Program (KYCX20_1489). We also thank for the experimental support from the experiment center for science and technology, Nanjing University of Chinese Medicine. We also thank the support of HCC organoids model by Zhongshan Hospital of FuDan University. The research is also financially supported by the "Innovative and Entrepreneurial Team" Program of Jiangsu Province (2020). And our team is leaded by Prof. Ming Zhao, Nanjing University of Chinese Medicine. The graphical abstract was created with BioRender.com. We really thank the scientific research platform provided by Prof. Tonghui Ma.

Appendix A. Supplementary data

Supplementary data to this article can be found online at https://doi.org/10.1016/j.redox.2022.102351.

References

[1] R.B. Damgaard, H.E. Jolin, M.E.D. Allison, S.E. Davies, H.L. Titheradge, A.N. J. McKenzie, D. Komander, OTULIN protects the liver against cell death, inflammation, fibrosis, and cancer, Cell Death Differ. 27 (2020) 1457–1474.
[2] J. Xu, Z. Wan, M. Tang, Z. Lin, S. Jiang, L. Ji, K. Gorshkov, Q. Mao, S. Xia, D. Cen, J. Zheng, X. Liang, X. Cai, N^6-methyladenosine-modified circRNA-sore sustains sorafenib resistance in hepatocellular carcinoma by regulating beta-catenin signaling, Mol. Cancer. 19 (2020) 163.
[3] H. Wang, Y. Liu, M. Xu, J. Cheng, Azido-galactose outperforms azido-mannose for metabolic labeling and targeting of hepatocellular carcinoma, Biomater. Sci. 7 (2019) 4166–4173.
[4] F. Caiado, D. Maia-Silva, C. Jardim, N. Schmolka, T. Carvalho, C. Reforco, R. Faria, B. Kolundzija, A.E. Simões, T. Baubec, C.R. Vakoc, M.G. da Silva, M.G. Manz, T. N. Schumacher, H. Norell, B. Silva-Santos, Lineage tracing of acute myeloid leukemia reveals the impact of hypomethylating agents on chemoresistance selection, Nat. Commun. 10 (2019) 4986.
[5] L. Huang, W. Cao, S. Ou, B. Yang, H. Zheng, J. Tang, J. Chen, Y.W. Hu, L. Zheng, Q. Wang, The long non-coding RNA PTTG3P promotes cell growth and metastasis via up-regulating PTTG1 and activating PI3K/AKT signaling in hepatocellular carcinoma, Mol. Cancer. 17 (2018) 93.
[6] Z. Yu, J. Guo, M. Hu, Y. Gao, L. Huang, Icaritin exacerbates mitophagy and synergizes with doxorubicin to induce immunogenic cell death in hepatocellular carcinoma, ACS Nano. 14 (2020) 4816–4828.
[7] P.M. Santos, L.H. Butterfield, Next steps for immune checkpoints in hepatocellular carcinoma, Gastroenterology. 155 (2018) 1684–1686.
[8] A.D. Garg, S. Martin, J. Golab, P. Agostinis, Danger signalling during cancer cell death: origins, plasticity and regulation, Cell Death Differ. 21 (2014) 26–38.
[9] N. Casares, M.O. Pequignot, A. Tesniere, F. Ghiringhelli, S. Roux, N. Chaput, E. Schmitt, A. Hamai, S. Hervas-Stubbs, M. Obeid, F. Coutant, D. Métivier, E. Pichard, P. Aucouturier, G. Pierron, C. Garrido, L. Zitvogel, G. Kroemer, Caspase-dependent immunogenicity of doxorubicin-induced tumor cell death, J. Exp. Med. 202 (2005) 1691–1701.
[10] A.D. Garg, A.M. Dudek-Peric, E. Romano, P. Agostinis, Immunogenic cell death, Int. J. Dev. Biol. 59 (2015) 131–140.
[11] J. Zhang, B. Zhang, X. Li, X. Han, R. Liu, J. Fang, Small molecule inhibitors of mammalian thioredoxin reductase as potential anticancer agents: an update, Med. Res. Rev. 39 (2019) 5–39.
[12] M. Bian, R. Fan, S. Zhao, W. Liu, Targeting the thioredoxin system as a strategy for cancer therapy: miniperspective, J. Med. Chem. 62 (2019) 7309–7321.
[13] C. Wen, H. Wang, X. Wu, L. He, Q. Zhou, F. Wang, S. Chen, L. Huang, J. Chen, H. Wang, W. Ye, W. Li, X. Yang, H. Liu, J. Peng, ROS-mediated inactivation of the PI3K/AKT pathway is involved in the antigastric cancer effects of thioredoxin reductase-1 inhibitor chaetocin, Cell Death Dis. 10 (2019) 1–16.
[14] B. Zhang, J. Zhang, S. Peng, R. Liu, X. Li, Y. Hou, X. Han, J. Fang, Thioredoxin reductase inhibitors: a patent review, Expert Opin. Ther. Pat. 27 (2017) 547–556.
[15] X. Chen, X. Chen, X. Zhang, L. Wang, P. Cao, V. Rajamanickam, C. Wu, H. Zhou, Y. Cai, G. Liang, Y. Wang, Curcuminoid B63 induces ROS-mediated paraptosis-like cell death by targeting TrxR1 in gastric cells, Redox Biol. 21 (2019) 101061.
[16] J. Zhang, D. Duan, A. Osama, J. Fang, Natural Molecules Targeting Thioredoxin System and Their Therapeutic Potential 34, Antioxid Redox Signal, 2020, pp. 1083–1107.
[17] T. San Lau, L.K.Y. Chan, G.C.W. Man, C.H. Wong, J.H.S. Lee, S.F. Yim, T. H. Cheung, I.A. McNeish, J. Kwong, Paclitaxel induces immunogenic cell death in

ovarian cancer via TLR4/IKK2/SNARE-dependent exocytosis, Cancer Immun. Res. 8 (2020) 1099–1111.
[18] S. Sen, S. Hufnagel, E.Y. Maier, I. Aguilar, J. Selvakumar, J.E. DeVore, V.M. Lynch, K. Arumugam, Z. Cui, J.L. Sessler, J.F. Arambula, Rationally designed redox-active Au(I) N-heterocyclic carbene: an immunogenic cell death inducer, J. Am. Chem. Soc. 142 (2020) 20536–20541.
[19] W. Xie, W. Ma, P. Liu, F. Zhou, Overview of thioredoxin system and targeted therapies for acute leukemia, Mitochondrion. 47 (2019) 38–46.
[20] E.S. Arnér, A. Holmgren, The thioredoxin system in cancer, Semin. Cancer Biol. 16 (2006) 420–426.
[21] A.S. Rothmeier, P. Marchese, B.G. Petrich, C. Furlan-Freguia, M.H. Ginsberg, Z. M. Ruggeri, W. Ruf, Caspase-1-mediated pathway promotes generation of thromboinflammatory microparticles, J. Clin. Invest. 125 (2015) 1471–1484.
[22] L. Huang, Y. Chen, B. Liang, B. Xing, G. Wen, S. Wang, X. Yue, C. Zhu, J. Du, X. Bu, A furanyl acryl conjugated coumarin as an efficient inhibitor and a highly selective off-on fluorescent probe for covalent labelling of thioredoxin reductase, Chem. Commun. 50 (2014) 6987–6990.
[23] T.J. Mafireyi, M. Laws, J.W. Bassett, P.B. Cassidy, J.O. Escobedo, R.M. Strongin, A diselenide turn-on fluorescent probe for the detection of thioredoxin reductase, Angew. Chem. 132 (2020) 15259–15263.
[24] X. Zhu, C. Yuan, C. Tian, C. Li, F. Nie, X. Song, R. Zeng, D. Wu, X. Hao, L. Li, The plant sesquiterpene lactone parthenolide inhibits Wnt/β-catenin signaling by blocking synthesis of the transcriptional regulators TCF4/LEF1, J. Biol. Chem. 293 (2018) 5335–5344.
[25] D. Martinez Molina, R. Jafari, M. Ignatushchenko, T. Seki, E.A. Larsson, C. Dan, L. Sreekumar, Y. Cao, P. Nordlund, Monitoring drug target engagement in cells and tissues using the cellular thermal shift assay, Science. 341 (2013) 84–87.
[26] Y. Ma, D. Yin, J. Ye, X. Wei, Y. Pei, X. Li, G. Si, X. Chen, Z. Chen, Y. Dong, F. Zou, W. Shi, Q. Qiu, H. Qian, G. Liu, Discovery of potent inhibitors against P-glycoprotein-mediated multidrug resistance aided by late-stage functionalization of a 2-(4-(Pyridin-2-yl)phenoxy)pyridine analogue, J. Med. Chem. 63 (2020) 5458–5476.
[27] S. Bestetti, M. Galli, I. Sorrentino, P. Pinton, A. Rimessi, R. Sitia, I. Medraño-Fernandez, Human aquaporin-11 guarantees efficient transport of H_2O_2 across the endoplasmic reticulum membrane, Redox Biol. 28 (2020) 101326.
[28] V.V. Pak, D. Ezeriņa, O.G. Lyublinskaya, B. Pedre, P.A. Tyurin-Kuzmin, N. M. Mishina, M. Thauvin, D. Young, K. Wahni, S.A.M. Gache, Ultrasensitive genetically encoded indicator for hydrogen peroxide identifies roles for the oxidant in cell migration and mitochondrial function, Cell Metabol. 31 (2020) 642–653, e646.
[29] T. Zhou, X. Liang, P. Wang, Y. Hu, Y. Qi, Y. Jin, Y. Du, C. Fang, J. Tian, A hepatocellular carcinoma targeting nanostrategy with hypoxia-ameliorating and photothermal abilities that, combined with immunotherapy, inhibits metastasis and recurrence, ACS Nano. 14 (2020) 12679–12696.
[30] K. Inaba, M. Inaba, N. Romani, H. Aya, M. Deguchi, S. Ikehara, S. Muramatsu, R. M. Steinman, Generation of large numbers of dendritic cells from mouse bone marrow cultures supplemented with granulocyte/macrophage colony-stimulating factor, J. Exp. Med. 176 (1992) 1693–1702.
[31] L. Li, H. Knutsdottir, K. Hui, M.J. Weiss, J. He, B. Philosophe, A.M. Cameron, C. L. Wolfgang, T.M. Pawlik, G. Ghiaur, Human primary liver cancer organoids reveal intratumor and interpatient drug response heterogeneity, JCI Insight. 4 (2019) 2.
[32] N. Prior, P. Inacio, M. Huch, Liver organoids: from basic research to therapeutic applications, Gut. 68 (2019) 2228–2237.
[33] R. Liu, D. Shi, J. Zhang, X. Li, X. Han, X. Yao, J. Fang, Virtual screening-guided discovery of thioredoxin reductase inhibitors, Toxicol. Appl. Pharmacol. 370 (2019) 106–116.
[34] J. Yao, D. Duan, Z. Song, J. Zhang, J. Fang, Sanguinarine as a new chemical entity of thioredoxin reductase inhibitor to elicit oxidative stress and promote tumor cell apoptosis, Free Radic. Biol. Med. 152 (2020) 659–667.
[35] C. Wen, H. Wang, X. Wu, L. He, Q. Zhou, F. Wang, S. Chen, L. Huang, J. Chen, H. Wang, W. Ye, W. Li, X. Yang, H. Liu, J. Peng, ROS-mediated inactivation of the PI3K/AKT pathway is involved in the antigastric cancer effects of thioredoxin reductase-1 inhibitor chaetocin, Cell Death Dis. 10 (2019) 1–16.
[36] L. Yu, W. Chen, Q. Tang, K. Ji, Micheliolide inhibits liver cancer cell growth via inducing apoptosis and perturbing actin cytoskeleton, Cancer Manag. Res. 11 (2019) 9203–9212.
[37] P. Kong, K.N. Yu, M. Yang, W.A. Almahi, L. Nie, G. Chen, W. Han, Micheliolide enhances radiosensitivities of p53-deficient non-small-cell lung cancer via promoting HIF-1alpha degradation, Int. J. Mol. Sci. 21 (2020).
[38] D. Lee, I.M. Xu, D.K. Chiu, J. Leibold, A.P. Tse, M.H. Bao, V.W. Yuen, C.Y. Chan, R. K. Lai, D.W. Chin, D.F. Chan, T. Cheung, S. Chok, C. Wong, S.W. Lowe, I.O. Ng, C. C. Wong, Induction of oxidative stress through inhibition of thioredoxin reductase 1 Is an effective therapeutic approach for hepatocellular carcinoma, Hepatology 69 (2019) 1768–1786.
[39] J.J. Lemasters, Dying a thousand deaths: redundant pathways from different organelles to apoptosis and necrosis, Gastroenterology 129 (2005) 351–360.
[40] I. Tabas, D. Ron, Integrating the mechanisms of apoptosis induced by endoplasmic reticulum stress, Nat. Cell Biol. 13 (2011) 184–190.
[41] N. Casares, M.O. Pequignot, A. Tesniere, F. Ghiringhelli, S. Roux, N. Chaput, E. Schmitt, A. Hamai, S. Hervas-Stubbs, M. Obeid, F. Coutant, D. Métivier, E. Pichard, P. Aucouturier, G. Pierron, C. Garrido, L. Zitvogel, G. Kroemer, Caspase-dependent immunogenicity of doxorubicin-induced tumor cell death, J. Exp. Med. 202 (2005) 1691–1701.
[42] S.R. Woo, L. Corrales, T.F. Gajewski, Innate immune recognition of cancer, Annu. Rev. Immunol. 33 (2015) 445–474.
[43] M. Obeid, A. Tesniere, F. Ghiringhelli, G.M. Fimia, L. Apetoh, J.L. Perfettini, M. Castedo, G. Mignot, T. Panaretakis, N. Casares, D. Métivier, N. Larochette, P. van Endert, F. Ciccosanti, M. Piacentini, L. Zitvogel, G. Kroemer, Calreticulin exposure dictates the immunogenicity of cancer cell death, Nat. Med. 13 (2007) 54–61.
[44] R. Zappasodi, S.M. Pupa, G.C. Ghedini, I. Bongarzone, M. Magni, A.D. Cabras, M. P. Colombo, C. Carlo-Stella, A.M. Gianni, M. Di Nicola, Improved clinical outcome in indolent B-cell lymphoma patients vaccinated with autologous tumor cells experiencing immunogenic death, Cancer Res. 70 (2010) 9062–9072.
[45] H. Zhu, Y. Shan, K. Ge, J. Lu, W. Kong, C. Jia, Oxaliplatin induces immunogenic cell death in hepatocellular carcinoma cells and synergizes with immune checkpoint blockade therapy, Cell. Oncol. 43 (2020) 1203–1214.
[46] V. Lai, S.Y. Neshat, A. Rakoski, J. Pitingolo, J.C. Doloff, Drug delivery strategies in maximizing anti-angiogenesis and anti-tumor immunity, Adv. Drug Deliv. Rev. (2021) 113920.
[47] H. Liu, L. Chen, C. Xu, Z. Li, H. Zhang, X. Zhang, W. Tan, Recent progresses in small-molecule enzymatic fluorescent probes for cancer imaging, Chem. Soc. Rev. 47 (2018) 7140–7180.
[48] S. Urig, K. Becker, On the potential of thioredoxin reductase inhibitors for cancer therapy, Semin. Cancer Biol. 16 (2006) 452–465.
[49] J. Zhang, X. Li, X. Han, R. Liu, J. Fang, Targeting the thioredoxin system for cancer therapy, Trends Pharmacol. Sci. 38 (2017) 794–808.
[50] L. Freire Boullosa, J. Van Loenhout, T. Flieswasser, J. De Waele, C. Hermans, H. Lambrechts, B. Cuypers, K. Laukens, E. Bartholomeus, V. Siozopoulou, W.H. De Vos, M. Peeters, E.L.J. Smits, C. Deben, Auranofin reveals therapeutic anticancer potential by triggering distinct molecular cell death mechanisms and innate immunity in mutant p53 non-small cell lung cancer, Redox Biol. 42 (2021) 101949.
[51] X. Zhu, Z. Yu, L. Feng, L. Deng, Z. Fang, Z. Liu, Y. Li, X. Wu, L. Qin, R. Guo, Y. Zheng, Chitosan-based nanoparticle co-delivery of docetaxel and curcumin ameliorates anti-tumor chemoimmunotherapy in lung cancer, Carbohydr. Polym. 268 (2021) 118237.
[52] R. Pisa, T.M. Kapoor, Chemical strategies to overcome resistance against targeted anticancer therapeutics, Nat. Chem. Biol. 16 (2020) 817–825.
[53] K. Anestål, E.S. Arnér, Rapid induction of cell death by selenium-compromised thioredoxin reductase 1 but not by the fully active enzyme containing selenocysteine, J. Biol. Chem. 278 (2003) 15966–15972.
[54] M. Cebula, E.E. Schmidt, E.S. Arnér, TrxR1 as a potent regulator of the Nrf2-Keap1 response system, Antioxid. Redox Signal. 23 (2015) 823–853.
[55] V.M. Labunskyy, V.N. Gladyshev, Role of reactive oxygen species-mediated signaling in aging, Antioxid. Redox Signal. 19 (2013) 1362–1372.
[56] V.I. Sayin, M.X. Ibrahim, E. Larsson, J.A. Nilsson, P. Lindahl, M.O. Bergo, Antioxidants accelerate lung cancer progression in mice, Sci. Transl. Med. 6 (2014) 215–221.
[57] H. Sies, D.P. Jones, Reactive oxygen species (ROS) as pleiotropic physiological signalling agents, Nat. Rev. Mol. Cell Biol. 21 (2020) 363–383.
[58] G. Csordás, D. Weaver, G. Hajnóczky, Endoplasmic reticulum–mitochondrial contactology: structure and signaling functions, Trends Cell Biol. 28 (2018) 523–540.
[59] U. Food, D. Administration, FDA Approves Lenvatinib for Unresectable Hepatocellular Carcinoma, Silver Spring, US Department of Health and Human Services, 2018.
[60] G. Wei, L. Huang, Y. Jiang, Y. Shen, Z. Huang, Y. Huang, X. Sun, C. Zhao, Lenvatinib-zinc phthalocyanine conjugates as potential agents for enhancing synergistic therapy of multidrug-resistant cancer by glutathione depletion, Eur. J. Med. Chem. 169 (2019) 53–64.
[61] Y. Guo, J. Xu, Q. Du, Y. Yan, D.A. Geller, IRF2 regulates cellular survival and Lenvatinib-sensitivity of hepatocellular carcinoma (HCC) through regulating β-catenin, Transl. Oncol. 14 (2021) 101059.
[62] Z. Zhao, D. Zhang, F. Wu, J. Tu, J. Song, M. Xu, J. Ji, Sophoridine suppresses lenvatinib-resistant hepatocellular carcinoma growth by inhibiting RAS/MEK/ERK axis via decreasing VEGFR2 expression, J. Cell Mol. Med. 25 (2021) 549–560.
[63] J. Xu, Q. Cheng, E.S. Arnér, Details in the catalytic mechanism of mammalian thioredoxin reductase 1 revealed using point mutations and juglone-coupled enzyme activities, Free Radic. Biol. Med. 94 (2016) 110–120.
[64] S. Sun, W. Xu, H. Zhou, Y. Zhang, J. Zhang, X. Li, B. Li, K. Ma, J. Xu, Efficient purification of selenoprotein thioredoxin reductase 1 by using chelating reagents to protect the affinity resins and rescue the enzyme activities, Process Biochem. 101 (2021) 256–265.
[65] Y. Zhang, S. Sun, W. Xu, R. Yang, Y. Yang, J. Guo, K. Ma, J. Xu, Thioredoxin reductase 1 inhibitor shikonin promotes cell necroptosis via SecTRAPs generation and oxygen-coupled redox cycling, Free Radic. Biol. Med. 180 (2022) 52–62.
[68] S. Sun, W. Xu, Y. Zhang, Y. Yang, Q. Ma, J. Xu, Menadione inhibits thioredoxin reductase 1 via arylation at the Sec498 residue and enhances both NADPH oxidation and superoxide production in Sec498 to Cys498 substitution, Free Radic. Biol. Med. 172 (2021) 482–489.
[69] Y. Yang, S. Sun, W. Xu, Y. Zhang, R. Yang, K. Ma, J. Zhang, J. Xu, Piperlongumine inhibits thioredoxin reductase 1 by targeting selenocysteine residues and sensitizes cancer cells to erastin, Antioxidants 11 (2022) 710.